

UCSF

UC San Francisco Previously Published Works

Title

Ultrasound frequency-controlled microbubble dynamics in brain vessels regulate the enrichment of inflammatory pathways in the blood-brain barrier

Permalink

<https://escholarship.org/uc/item/05s286j3>

Journal

Nature Communications, 15(1)

ISSN

2041-1723

Authors

Guo, Yutong

Lee, Hohyun

Kim, Chulyong

et al.

Publication Date

2024

DOI

10.1038/s41467-024-52329-y

Peer reviewed


Ultrasound frequency-controlled microbubble dynamics in brain vessels regulate the enrichment of inflammatory pathways in the blood-brain barrier

Received: 20 November 2023

Accepted: 4 September 2024

Published online: 13 September 2024

 Check for updates

Yutong Guo^{1,2}, Hohyun Lee¹, Chulyong Kim¹, Christian Park³, Akane Yamamichi⁴, Pavlina Chuntova⁴, Marco Gallus⁴, Miguel O. Bernabeu^{5,6}, Hideho Okada^{4,7}, Hanjoong Jo^{3,8} & Costas Arvanitis^{1,3} 


Microbubble-enhanced ultrasound provides a noninvasive physical method to locally overcome major obstacles to the accumulation of blood-borne therapeutics in the brain, posed by the blood-brain barrier (BBB). However, due to the highly nonlinear and coupled behavior of microbubble dynamics in brain vessels, the impact of microbubble resonant effects on BBB signaling and function remains undefined. Here, combined theoretical and prospective experimental investigations reveal that microbubble resonant effects in brain capillaries can control the enrichment of inflammatory pathways that are sensitive to wall shear stress and promote differential expression of a range of transcripts in the BBB, supporting the notion that microbubble dynamics exerted mechanical stress can be used to establish molecular, in addition to spatial, therapeutic windows to target brain diseases. Consistent with these findings, a robust increase in cytotoxic T-cell accumulation in brain tumors was observed, demonstrating the functional relevance and potential clinical significance of the observed immuno-mechano-biological responses.

A major obstacle towards attaining sufficient accumulation of blood-borne therapeutics in the brain is posed by the blood-brain barrier (BBB) – a specialized neurovascular unit evolved to keep the brain “safe” by closely monitoring and regulating the transport of macromolecules and cells^{1–5}. Circulating microbubbles (MB) upon ultrasound (US) exposure (sonication) can exert mechanical stress (i.e., by expanding during peak negative and contracting during peak positive pressure) in brain vessels to trigger a range of responses, including local increase in the BBB permeability^{6–8} and activation of inflammatory signaling and phenotypes^{9–11}. These transient phenotypic changes

have led to the development of highly potent targeted drug delivery strategies for a wide range of brain diseases, including cancer and Alzheimer’s^{12–15}. Increasing evidence suggests that the above responses could act synergistically, too. In brain tumors, for example, they can enrich both the accumulation of immune adjuvants and the immune landscape in the brain tumor microenvironment to target more effectively aggressive brain tumors, such as glioblastomas^{16–19}. However, emerging clinical evidence suggests that it may also lead to the accumulation of CD4⁺ lymphocytes in the brain tumor microenvironment²⁰, which have been associated with unfavorable

¹Georgia Institute of Technology, Woodruff School of Mechanical Engineering, Atlanta, USA. ²Stanford University, Department of Radiology, Stanford, USA.

³Georgia Institute of Technology and Emory University, Coulter Department of Biomedical Engineering, Atlanta, USA. ⁴University of California San Francisco, Department of Neurological Surgery, San Francisco, USA. ⁵The University of Edinburgh, Centre for Medical Informatics, Usher Institute, Edinburgh, United Kingdom. ⁶The University of Edinburgh, The Bayes Centre, Edinburgh, United Kingdom. ⁷Parker Institute for Cancer Immunotherapy, San Francisco, USA.

⁸Emory University, Department of Medicine, Atlanta, USA.  e-mail: costas.arvanitis@gatech.edu

prognosis in glioblastoma²¹, and may thus dampen any potential therapeutic benefits. Likewise, research in Alzheimer's mouse models has alluded to the possibility of MB-enhanced US, alone or in combination with therapeutic agents, to augment microglia's ability to clear toxic proteins and improve cognitive function^{22–25}. However, it is also recognized that microglial activation can fuel disease progression by promoting neuronal dysfunction and damage^{26,27}. Therefore, identifying strategies to control and, ideally, selectively activate these responses is important for defining and optimizing therapeutic windows to improve treatment efficacy, while minimizing side effects^{15,28}.

Toward this goal, extended research over the past years has shown that the strength of MB acoustic emissions (i.e., Harmonics and Ultra-Harmonics), which provide a good proxy to the strength of the MB oscillations and exerted mechanical stress in the brain vessels²⁹, correlates well with changes in BBB permeability¹⁴. As a result, the MB emissions have formed the basis for developing closed-loop methods to fine-tune the US excitation amplitude and promote desirable changes in the BBB phenotype¹⁴. Despite the ability of such methods to mitigate major safety concerns¹⁵, increasing evidence suggests that the US amplitude lacks the ability to differentially impact the observed biological responses^{28,30,31}. This inevitably leads to a very narrow treatment window and therapeutic index between efficacy and neurotoxicity^{14,32}. By contrast, due to MB resonance effects, tuning the US excitation frequency can lead to a range of behaviors that can critically shape the exerted stress and (micro)streaming patterns in the surrounding fluid³³ and potentially the observed responses and treatment window. However, due to the complexity of the MB dynamics in brain vessels, the strong dependence of their resonance characteristics to the MB size and shell composition³⁴, and the lack of *in vivo* methods to directly assess the MB-vessel interactions³⁵, the impact of US frequency on MB-induced mechanical stress and observed biological responses has not been uniquely determined^{36–42}. Consequently, the principles to design MBs and US excitation pulses to harness MB resonant effects and fine-tune the exerted mechanical stress to elicit desirable changes in the BBB signaling and function remain poorly defined^{14,43}.

We hypothesize that MB resonant effects in brain capillaries can transiently modulate the BBB signaling and function and allow the establishment of molecular, in addition to spatial, therapeutic windows to improve the accumulation of blood-borne therapeutics in the brain. To test our hypothesis and refine our understanding of the impact of MB resonant effects on the exerted mechanical stress on the brain vessels and the ability to promote distinct transcriptional and functional changes in the BBB, we combined high-fidelity mathematical modeling of MB dynamics in vessels with prospective experimental investigations in mice. For the latter, we assessed the changes in the BBB phenotype for different US excitation parameters (frequency and pressure) and MB properties (size and shell) at different time points (8 and 24 h) using dynamic contrast-enhanced MRI, RNA sequencing, and immunofluorescence. Finally, based on the observed BBB phenotypic changes, we assessed the potential of US frequency and, by extension, of MB resonant effects to selectively alter the trafficking of epidermal growth factor receptor variant III (EGFRvIII) chimeric antigen receptor (CAR) T cells in orthotopic EGFRvIII murine glioma tumors.

Results

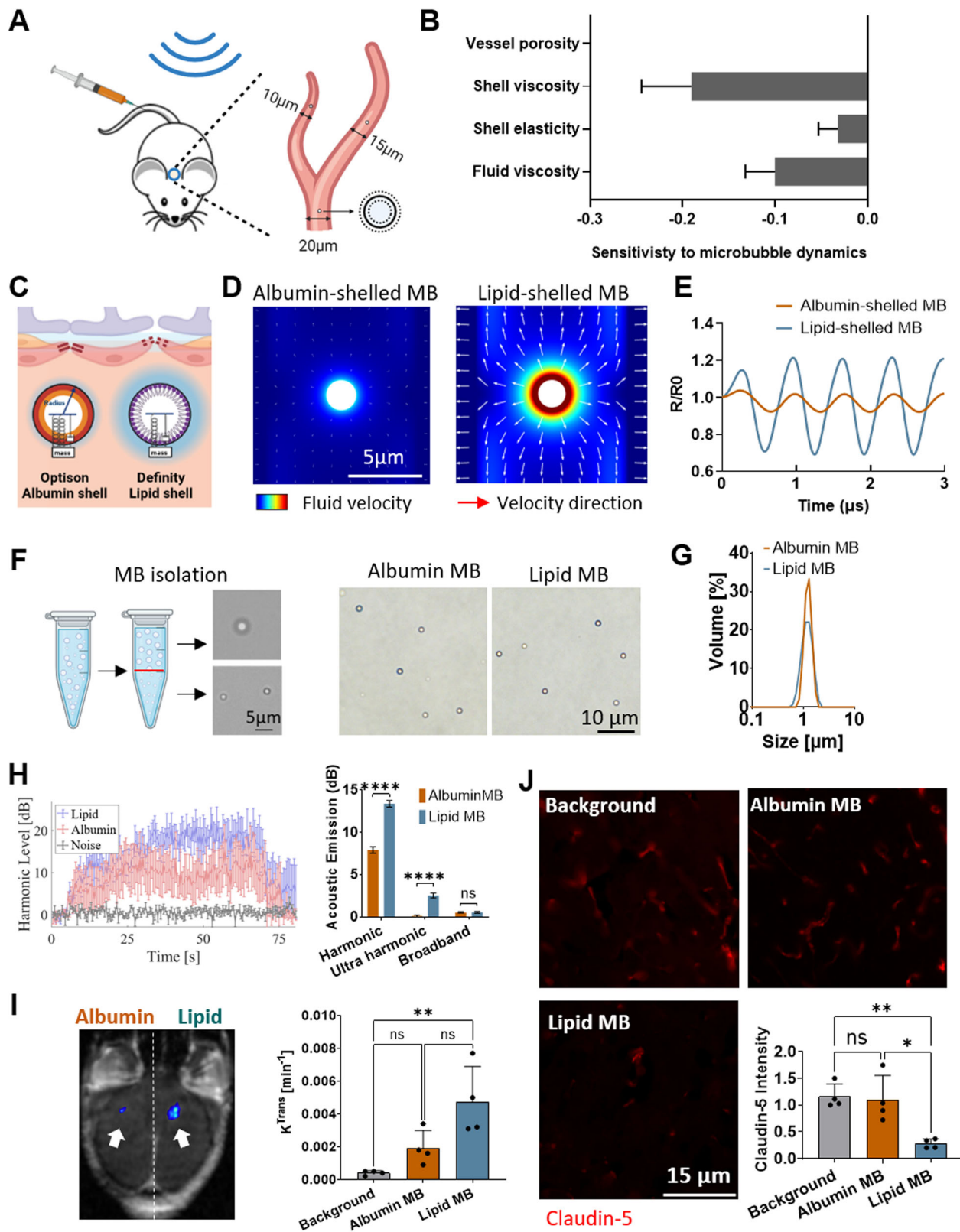
Microbubbles with a more elastic shell are more potent in increasing the blood-brain barrier permeability

Studying the highly non-linear MB dynamics in brain vessels to determine how they impact the BBB signaling and function is profoundly challenging, as current imaging methods cannot resolve the microscale oscillations in time and space behind the optically opaque tissues³⁵. Hence, to mitigate challenges associated with resolving the MB dynamics in brain capillaries and gain mechanistic insights on the

interaction between MB, US, and the forces exerted on the vessel wall, it is critical to develop and validate mathematical modeling of MB dynamics in brain vessels. To better capture the fluid dynamics and its interaction with the vessel wall we considered the vessel and surrounding brain as porous material. Furthermore, we aimed to prospectively assess the biological significance of model predictions in animal experiments, which is currently missing from current modeling work^{44–50}. First, to understand the relative importance of the parameters involved in the MB-vessel system, we conducted a parametric sensitivity analysis and found that the properties of the MB shell significantly affect the dynamics of MB inside vessels (Fig. 1A, B). In our simulations, we employed vessels ranging from 5–20 μm in size as past investigations have shown more pronounced biological responses to MB oscillations in this size range^{51,52}. Then, to further study the effect of MB shell properties on their dynamics and the resulting bioeffect, we modeled two commercially available and well-characterized MBs, Optison (GE Healthcare) and Definity (Lantheus Medical Imaging)⁵³. Optison MB has a thicker and stiffer shell made of human serum albumin, while the shell of Definity MB is made of a lipid, which is more elastic (Fig. 1C and Supplementary Table 1). While the MB dynamics in our model are based on the Marmottant model, which has been validated using lipid shell MB that is characterized by a buckled and an elastic region⁵⁴, it has been shown that albumin-shelled MB follows a similar behavior⁵⁵. Hence, the same MB modeling assumptions can be used for both agents, especially for low amplitude oscillations⁵⁶. Under these conditions, the model indicated that the MB with a more elastic shell has stronger relative oscillation amplitude, $\Delta R/R_0$, (3% and 16% changes of their resting size for albumin and lipid shelled MB, respectively) under the same acoustic pressure (Fig. 1D, E), suggesting that MBs with different shell properties can exert different stress and, by extension, impact the BBB signaling and function differently.

To test our model predictions, which expands current thinking that suggests the MB total gas volume is sufficient to predict the MB bioeffects³⁸, we conducted experiments on healthy mouse brains using equal doses of size-selected lipid and albumin-shelled MB (Fig. 1F, G) (i.e., similar gas volume) and a calibrated US-guided Focused Ultrasound (USgFUS) system (Supplementary Fig. 1A)¹⁶. We performed microbubble-enhanced focused ultrasound (MB-FUS) treatment in the right and left hemispheres of the same mouse with concurrent administration of lipid or albumin-shelled MBs (2 μm , 5×10^8 MBs/ml), respectively, using 175 kPa peak negative focal pressure (PNP) with 1.5 MHz FUS transducer (see Methods for detailed parameters and pressure measurements). Since albumin-shelled MB have a shorter circulation half-life compared to lipid-shelled MB (Supplementary Fig. 1B), we administered both MBs using infusion to ensure the MB concentration was constant throughout the sonication period. During the sonication, we monitored the MB acoustic emissions using passive acoustic monitoring. The acoustic emissions confirmed that the kinetics of the two MBs were comparable and revealed that the harmonic emissions from the lipid-shelled MB were stronger compared to those from albumin-shelled MB (1.7-fold in dB, $p < 0.0001$) (Fig. 1H). As we observed minimal broadband emissions for these two MB (less than 1–2 pulses per sonication), we concluded that our findings are primarily associated with stable MB oscillation. Together, these findings support the model predictions and indicate that MBs with a more elastic shell have more vigorous oscillation inside brain vessels, as evidenced by the stronger acoustic emissions.

Next, to assess the impact of MB with different shell properties on BBB permeability, we employed dynamic contrast-enhanced MR imaging (DCE-MRI) and measured the changes in K^{trans} shortly after the MB-FUS treatment. These measurements (i.e., K^{trans} values) indicate changes in vascular permeability assuming the same level of perfusion across animals. The K^{trans} values were significantly higher in the lipid-shelled MB group (12-fold, $p = 0.005$) but not in the albumin-shelled MB group as compared to the non-FUS treated region, demonstrating



that the more elastic MB has a higher impact on BBB permeability (Fig. 1I). We confirmed these findings by assessing the expression of Claudin-5, a tight junction protein which is involved in restricting paracellular transport across the BBB³⁷, and found that its expression was significantly down-regulated in the brain region sonicated with lipid-shelled MB compared to the region sonicated with albumin-shelled MB (4-fold, $p = 0.01$) (Fig. 1J).

Furthermore, we assessed the effect of MB size on BBB permeability and found that using the 2 μm lipid-shelled MB led to stronger oscillations (11% and 16% changes of their resting size for 1 μm and 2 μm MB, respectively, Supplementary Fig. 3A), stronger harmonic emissions (7.3-fold, $p < 0.0001$, Supplementary Fig. 3B–D), and higher K^{trans} values (2-fold, $p = 0.017$, Supplementary Fig. 3E, F), compared to 1 μm lipid-shelled MB using the same acoustic settings (1.5 MHz, 175 kPa

Fig. 1 | MBs with more elastic shell are more potent at eliciting BBB physical and molecular changes. **A** Mathematical modeling of microbubble dynamics inside a vessel. Schematic created with BioRender.com. **B** Sensitivity analysis of model parameters to the microbubble oscillation amplitude inside vessels of size 5–20 μm ($n = 4$). Bound of the box plot shows minima and maxima. **C** Two microbubbles, Optison and Definity, with different sizes and shell materials, were studied. Schematic created with BioRender.com. **D** MB oscillation inside a 15 μm vessel (1.5 MHz, 175 kPa - peak negative). **E** Relative MB oscillation amplitude, R/RO, for lipid and albumin-shelled microbubbles inside a 15 μm vessel (1.5 MHz, 175 kPa - peak negative). **F** Representative microscope images of microbubbles that were isolated using buoyancy force before each experiment. MB was characterized before every experiment. Schematic created with BioRender.com. **G** Size distribution of selected monodispersed lipid and albumin-shelled MBs. **H** Acoustic

emission from the MB oscillations. *P*-values were determined by two-way analysis of variance (ANOVA) and adjusted using Bonferroni correction. Plots show means \pm SD ($n = 644$). Measurements were taken from individual sonication.

I Representative Ktrans color map (left) and quantification (right) of Ktrans value for lipid and albumin-shelled microbubbles. Measurements were taken from distinct samples. Plots show means \pm SD ($n = 4$). *P*-values were determined by one-way analysis of variance (ANOVA) and adjusted using Bonferroni correction. (Background vs Lipid MB, $p = 0.005$). **J** Representative fluorescent microscopy data and quantification of Claudin-5 expression at 1 h after MB-FUS. Measurements were taken from distinct samples. Plots show means \pm SD ($n = 4$). *P*-values were determined by one-way analysis of variance (ANOVA) and adjusted using Bonferroni correction. (Background vs Lipid MB, $p = 0.007$; Albumin MB vs Lipid MB, $p = 0.0103$) n.s. no significance $P > 0.05$, * $P \leq 0.05$, ** $P \leq 0.01$, **** $P \leq 0.0001$.

PNP) (Supplementary methods 3). These findings are in agreement with past observations that have demonstrated the role of MB size on the observed changes in BBB phenotype⁵⁸. Taken together, the alignment of our mathematical predictions with experimental data not only underscores the capability of the mathematical model to capture the interactions between MB and brain vessels but also indicates that MB dynamics in brain vessels are significantly influenced by the MB properties; with larger MB with more elastic shell being more potent at eliciting physical and molecular changes in the BBB.

Ultrasound frequency can be tuned to elicit differential gene expression in the BBB

Having established that 2 μm lipid-shelled MB leads to strong MB oscillation and robust changes in BBB permeability, we selected this MB type and size to further assess the impact of US frequency on BBB signaling and function. As before, our analysis started with mathematical modeling followed by experimental investigations designed to assess the biological significance of the model predictions regarding the MB dynamics within the brain vessels. First, we conducted sensitivity analysis by varying the excitation frequency over clinically relevant frequencies (from 0.5 to 5 MHz; Fig. 2A). The model clearly demonstrated the presence of MB resonant effects inside vessels (≈ 1 MHz; Fig. 2B). Interestingly, at frequencies adjacent to the MB resonance frequency inside the vessel (0.5 MHz and 1.5 MHz), where the relative MB oscillation amplitude is comparable (Fig. 2B), the wall shear stress (WSS) is 2-fold higher during MB expansion and 1.3-fold higher during MB contraction for the higher frequency (1.5 MHz) as compared to the lower frequency (0.5 MHz) (Fig. 2D, H). Mechanistically, this occurs because frequencies just above resonance lead to higher fluid vorticity and, therefore, higher WSS (Fig. 2C, H). Also because the baseline WSS in capillaries can be negligible compared to WSS generated by the MB, the observed changes are primarily related to MB exerted stress and not due to distortion of normal blood flow⁵⁹. At frequencies much higher than resonance, this effect is offset by the much smaller MB displacements ($\Delta R/R$). To better understand these findings, we performed an extended parametric sensitivity analysis to assess the influence of key parameters on the WSS induced by MB oscillation (Fig. 2E and Supplementary Fig. 4). Our sensitivity analysis reveals that both the MB shell viscosity and fluid viscosity can substantially affect the WSS and reduce its level by up to 1.4 kPa, aligning it with physiological levels, without altering its frequency-dependent trend (Fig. 2E and Supplementary Fig. 4). To explore if our observations from single microbubble oscillation inside a vessel are applicable to multiple microbubbles, we also modeled the oscillation of two microbubbles inside vessels of size 5–20 μm . While our current implementation is limited to relatively weak bubble-bubble interactions (i.e., it excludes microbubble coalescence), it demonstrates that despite the differences in the microstreaming pattern in the surrounding fluid (the oscillation amplitude of each MB decreases, whereas the overall WSS increases; Fig. 2F, G), for microbubble distances down to 3 μm , the

frequency-dependent trend of microbubble oscillation and WSS is consistent with the findings from the single microbubble (Fig. 2H, I and Supplementary Fig. 4E–G). Crucially, these observations lead to the following testable hypothesis: 1.5 MHz excitation frequency can activate the BBB signaling and functional changes that are responsive to WSS more effectively than 0.5 MHz.

Testing the above hypothesis is not trivial, as there are several technical and biological challenges, including (i) attaining the same intracranial focal pressure at both frequencies, (ii) ensuring the pressures are below the threshold for inertial cavitation, (iii) getting narrow MB distribution (i.e., wide MB distribution contributes to a broader range of behaviors within an MB population that in turn overshadows resonant effects), and (iv) accounting for biological variability and vascular heterogeneity. Due to these challenges, the impact of US frequency on MB-induced mechanical stress and observed biological responses has yet to be determined. To overcome these challenges, we employed a calibrated USgFUS with a fundamental frequency at 0.5 MHz that can also be operated at 1.5 MHz, while accounting for insertion loss by the skull (experimental measurements) and standing wave formation (mathematical modeling) (Supplementary Fig. 5). To determine the pressures that are safe for both frequencies, we examined pressures ranging from 125 kPa to 175 kPa (peak negative focal pressure) using monodispersed 2 μm lipid MBs. We found that 175 kPa resulted in a higher occurrence of broadband signals compared to lower pressures (no broadband signal detected for 125 kPa), yet it did not cause any hemorrhage and damage as shown in hematoxylin and eosin (H&E) staining (Fig. 3A, B, E and Supplementary Fig. 6D). With these considerations in mind, we analyzed the K^{trans} value following the sonication and found a similar level at both frequencies (Fig. 3C, D and Supplementary Fig. 6A–C), suggesting that the MB oscillation amplitude $\Delta R/R$ is critical for opening the BBB.

To further investigate the impact of US frequency and MB dynamics on broader transcriptome changes in brain vessels, we performed bulk RNA sequencing (RNAseq) analysis of endothelial cells (EC) enriched by isolating PECAM-1 positive cells from all cell populations of the brain in healthy mice at 8- and 24-hours post-sonication. While several studies have shown changes in the BBB transcriptome in mixed brain cells in response to US^{11,28,30,31,60}, we focused on testing transcriptome changes occurring specifically in ECs, due to their unique sensitivity to mechanical stresses⁶¹ and the strong MB-induced mechanical stress exerted on the ECs, as indicated by our model (Fig. 2). For the MB-FUS experiments, we selected pressures of 150 kPa and 175 kPa for both 0.5 MHz and 1.5 MHz frequencies. The 150 kPa setting was chosen to minimize the likelihood of microbubble collapse, while the 175 kPa, although may lead to slightly increased broadband emission, remains relatively safe based on the H&E staining (Fig. 3A, B, E). The RNAseq analysis showed a significant upregulation of 181 genes in the 1.5 MHz frequency group compared to the 0.5 MHz group when treated at 150 kPa, and this number increased to 348 genes at 175 kPa pressure, at the 8-hour time point after the MB-FUS

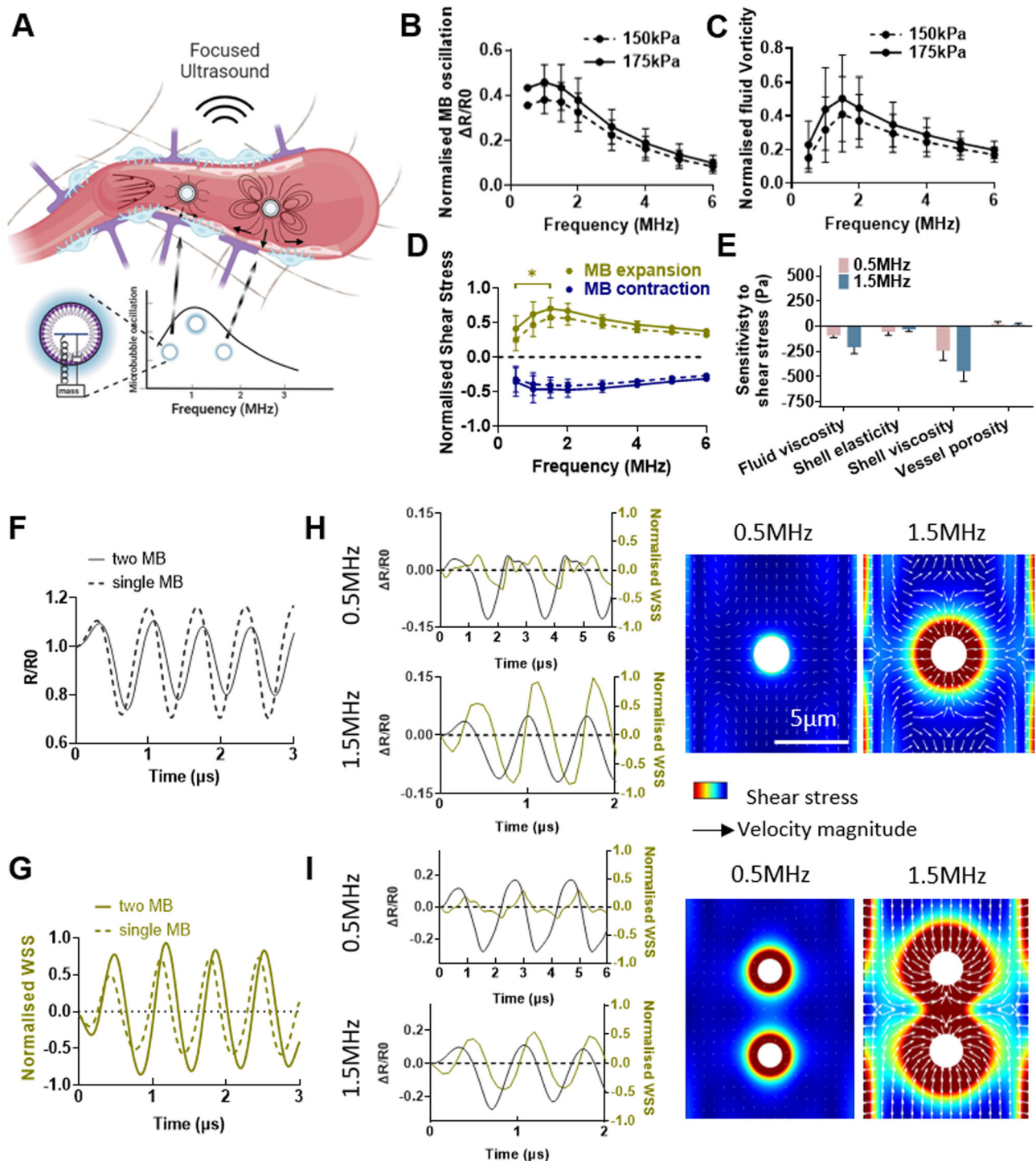


Fig. 2 | Mathematical modeling of microbubble dynamics inside vessels and the mechanical forces exerted on the vessel wall. Schematic created with BioRender.com. **A** Schematic illustration of microbubble oscillation that is excited with different ultrasound frequencies inside brain vessel. **B** Relative oscillation amplitude of lipid MB inside vessels of size 5–20 μm . Plots show means \pm SEM ($n = 4$). **C** Normalized fluid vorticity inside vessels caused by microbubble oscillation excited at different frequencies inside vessels of size 5–20 μm . Plots show means \pm SEM ($n = 4$). **D** Vessel wall shear stress exerted by microbubble oscillation inside vessels of size 5–20 μm during the expansion and contraction phase. Plots

show means \pm SEM ($n = 4$). **E** Sensitivity analysis of model parameters to the WSS inside vessels of size 5–20 μm . Plots show means \pm SD ($n = 4$). **F** Microbubble dynamics of a single and two 2 μm Definity microbubbles excited at 1.5 MHz inside a 10 μm vessel. **G** Vessel wall shear stress (WSS) exerted on the vessel wall by a single and two 2 μm Definity microbubbles excited at 1.5 MHz inside a 10 μm vessel. **H** Microbubble dynamics of a single 2 μm Definity microbubble excited at 0.5 MHz and 1.5 MHz inside a 10 μm vessel. **I** Microbubble dynamics of two 2 μm Definity microbubbles excited at 0.5 MHz and 1.5 MHz inside a 10 μm vessel.

treatment, indicating that the responses scale with pressure, in addition to frequency. As expected, the expression levels between two different frequency groups returned to similar levels 24 h after sonication, indicating that the changes at the transcriptomic level induced

by MB oscillation are transient (Fig. 4A, B, and Supplementary Fig. 7). In addition, the expression of genes associated with cell apoptosis did not show significant changes compared to the non-FUS-treated brains across all treatment groups, both 8 h and 24 h post-sonication, further

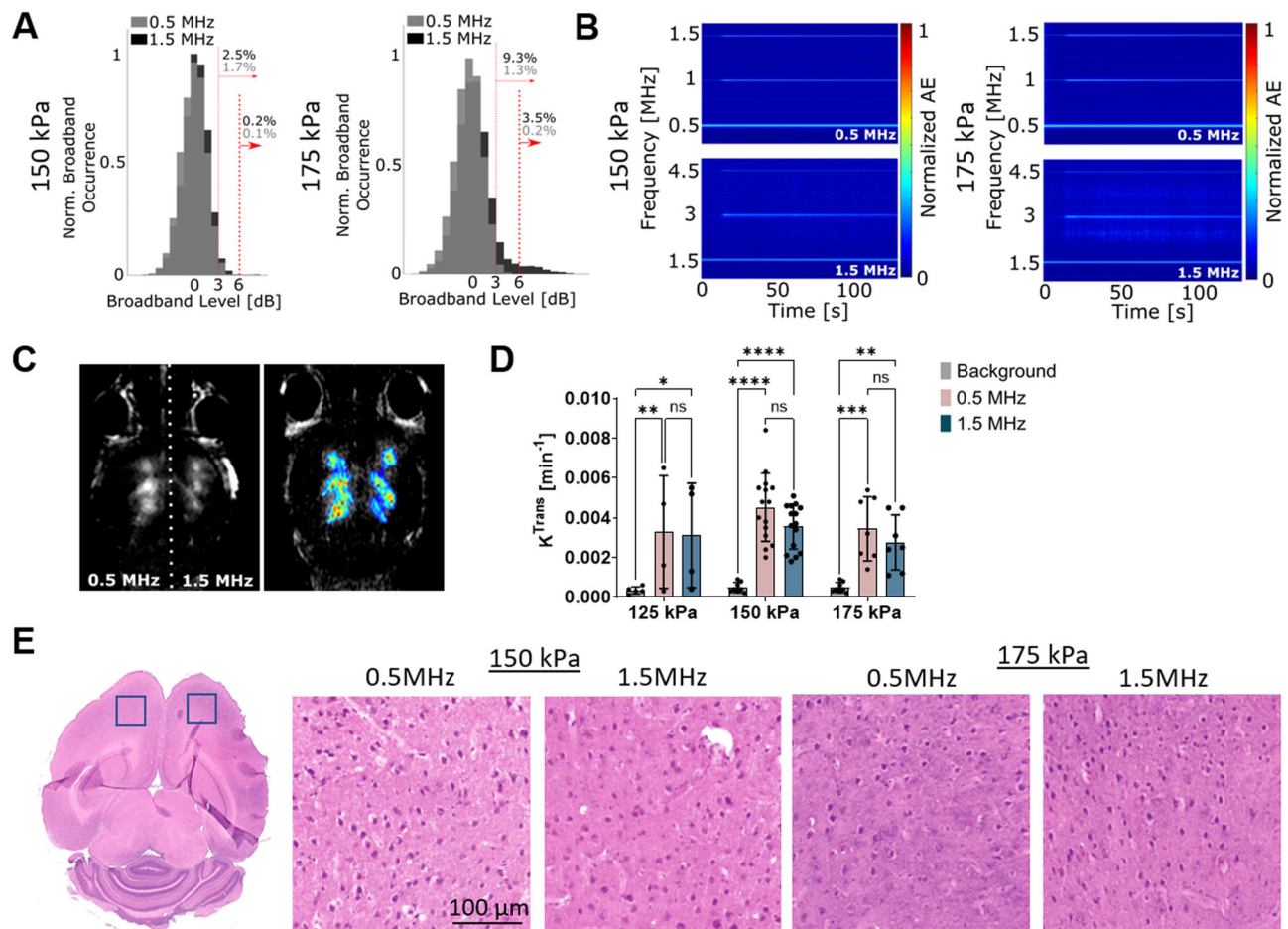


Fig. 3 | Impact of US frequency on the BBB permeability in the brains of healthy mice. **A** Broadband emission (> 3 dB) probability during MB-FUS sonication using 150 kPa and 175 kPa pressure. **B** Spectrogram during sonication using 150 kPa and 175 kPa pressure. Harmonic levels increased significantly following microbubble arrival to the brain after a bolus injection at $t = 10$ s. Minimal broadband emission was observed. Color bar normalized acoustic emission. **C** Representative K_{trans} color map for 0.5 MHz and 1.5 MHz frequency using 175 kPa. **D** Quantification of K_{trans} for 0.5 MHz and 1.5 MHz frequency.

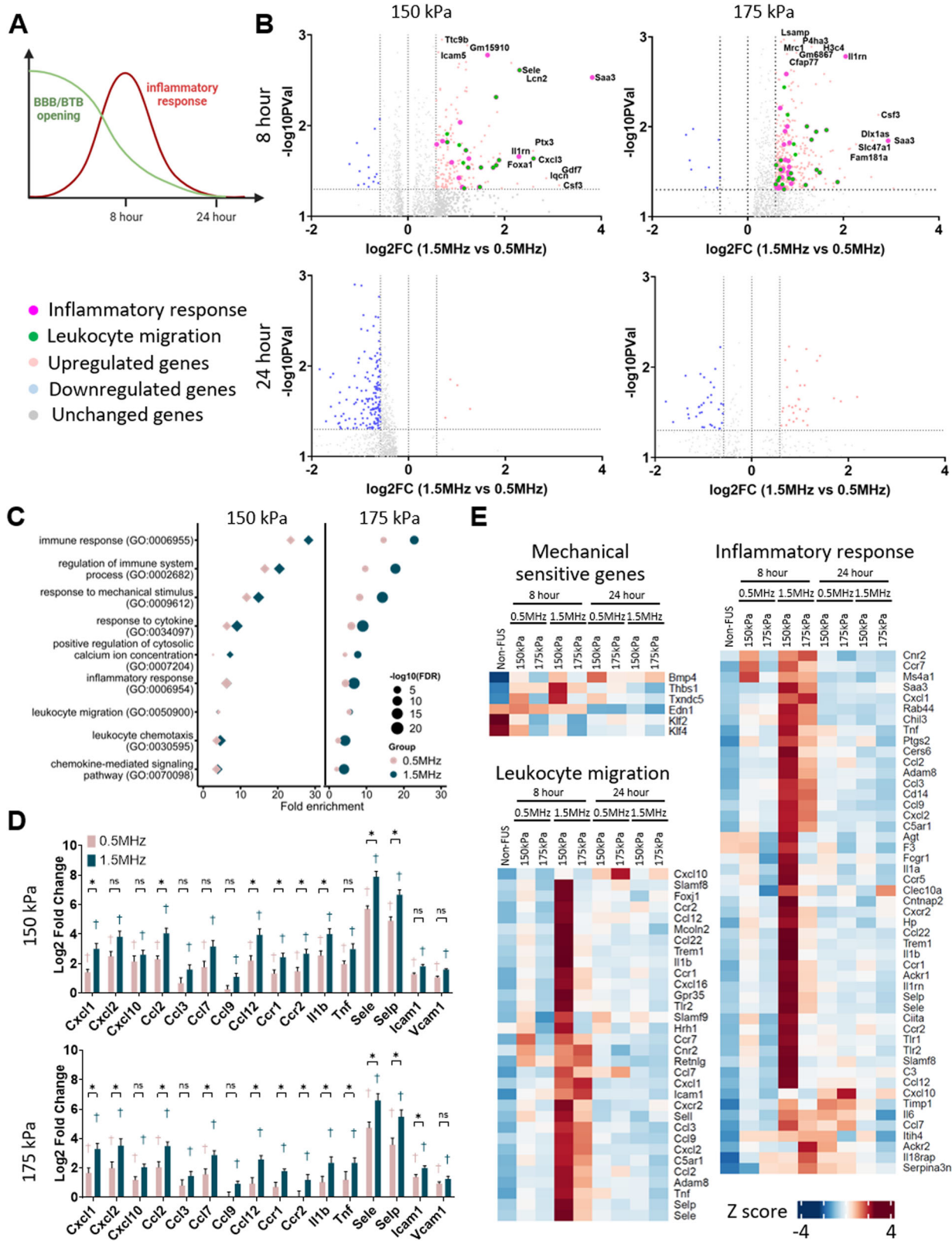
Measurements were taken from each sonicated location. Plots show means \pm SD ($n = 4$ for the 125 kPa group, $n = 15$ for the 150 kPa group, and $n = 7$ for the 175 kPa group). P -values were determined by one-way analysis of variance (ANOVA) and were adjusted using Bonferroni correction. n.s. no significance $P > 0.05$, $*P \leq 0.05$, $**P \leq 0.01$, $***P \leq 0.001$, $****P \leq 0.0001$. **E** Representative H&E staining images of the brain treated with 150 kPa and 175 kPa pressure. H&E staining was performed on three distinct samples for each experimental condition to confirm consistent results.

confirming that the treatment using the selected parameters does not promote cell death and can broadly consider as safe (Supplementary Fig. 7).

To understand the biological processes associated with the observed changes in transcripts, we performed unbiased gene ontology (GO) analysis. The GO analysis of RNA sequencing data revealed that the transcriptome changes in brain ECs caused by MB oscillation were associated with numerous significantly enriched pathways related to mechanical stimulus, cytokine signaling pathways, inflammatory responses, and leukocyte migration, for both 0.5 MHz and 1.5 MHz group (Fig. 4C). Interestingly, the GO analysis results indicated enrichment in pathways related to regulation of ion channels which are known to be involved in modulating calcium signaling in response to mechanical forces for MB-FUS treated groups (Fig. 4C). Remarkably, the 1.5 MHz group showed higher enrichment levels than the 0.5 MHz group, especially at 175 kPa pressure (Fig. 4C). We then further investigated the genes associated with the significantly enriched pathways. Firstly, we observed changes in the expression of mechanosensitive genes (Fig. 4E and Supplementary Fig. 8), indicating the presence of disturbed flow. Moreover, we observed a significant upregulation of transcripts related to inflammatory response and leukocyte migration in the 1.5 MHz group compared to the 0.5 MHz group at 8 h post MB-

FUS. While we observed increased gene expression at the lower pressure (150 kPa vs 175 kPa) at 8 h after MB-FUS, as compared to the control, most of them were not statistically significant (Fig. 4E, Supplementary Fig. 12). In addition, the GO analysis shows that the gene expressions that are significantly higher at lower pressure are not associated with the pathways related to mechanical stimulus, cytokine signaling pathways, inflammatory responses, and leukocyte migration. More specifically, 8 h following FUS treatment at 175 kPa, transcripts for the chemokines *Cxcl1*, *Cxcl2*, *Ccl2*, *Ccl7*, *Ccl12*, *Ccr1*, and *Ccr2* were significantly upregulated in the 1.5 MHz group compared to the 0.5 MHz group (Fig. 4D, E and Supplementary Tables 2, 3). Notably, we found several chemokines, including *Ccl3* and *Ccl9*, that were not upregulated in the 0.5 MHz group compared to the non-FUS control group but were significantly upregulated in the 1.5 MHz group at 175 kPa (Fig. 4D, E, and Supplementary Table 2, 3). Moreover, pro-inflammatory cytokines, including tumor necrosis factor (*Tnf*) and *Il6*, were not upregulated in the 0.5 MHz group as compared to the non-FUS control group but were significantly enhanced in the 1.5 MHz group at 8 h (Fig. 4D, E and Supplementary Tables 2, 3). A similar trend can be found for 150 kPa.

Notably, we observed a significant upregulation of E-selectin (*Sele*), P-selectin (*Selp*), and Intercellular adhesion molecule 1 (*Icam1*)



in the 1.5 MHz group compared to the 0.5 MHz group at 8 h (Fig. 4 D, E and Supplementary Tables 2, 3). These adhesion molecules are sensitive to shear stress and play a crucial role in regulating leukocyte-endothelial interactions and extravasation during inflammatory responses^{62–64}. To validate these findings from transcriptome analysis and confirm protein expression, we performed immunofluorescent staining. Our analysis revealed a 2.2-fold increase in

ICAM-1 expression in the 1.5 MHz group compared to the 0.5 MHz group at 150 kPa, and a 2.4-fold increase at 175 kPa (Fig. 5A, B). In addition, our findings revealed a significant upregulation of IBA-1 in the 1.5 MHz group compared to the 0.5 MHz group at 8 h post-treatment (at 150 kPa peak negative pressure). The increase in IBA-1, a marker for microglial activation, indicates enhanced immune response, providing additional evidence for the more pronounced

Fig. 4 | RNA sequencing of endothelial cells (ECs) in mouse brain tissue.

A Schematic illustration of the timelines for different bioeffects of MB-FUS. Schematic created with BioRender.com. **B** Volcano plots show gene expression changes in ECs exposed to 1.5 MHz and 0.5 MHz at 8 and 24 h after MB-FUS with different ultrasound pressures. Note the fold change shows the changes in the expression of all analyzed transcripts when microbubbles are excited at 1.5 MHz as compared to 0.5 MHz. *P*-values were determined by two-tailed unpaired *t* tests. **C** Unbiased gene-set enrichment analyses of genes that are significantly upregulated after MB-FUS with 1.5 MHz and 0.5 MHz frequencies compared to non-FUS treated control at 150 kPa and 175 kPa. **D** Log₂ fold change of the expression of selected transcripts after MB-FUS treatment compared to non-FUS treated group at 8 h post-treatment,

with 150 kPa and 175 kPa ultrasound pressure. The selected transcripts are related to inflammatory cytokines, chemokines, and vascular cell adhesion molecules. Measurements were taken from distinct samples. Plots show means \pm SD ($n = 6$). *P*-values were determined by two-tailed unpaired *t* tests. † Show statistically significant difference between the MB-FUS treatment group (0.5 MHz and 1.5 MHz) and the non-FUS treated group at 8 h post-treatment. * Show statistically significant difference between 0.5 MHz and 1.5 MHz at 8 h post-treatment. n.s. no significance, $P > 0.05$, † $P \leq 0.05^*$, $P \leq 0.05$. **E** Heatmap of the z score of genes sensitive to mechanical forces associated with leukocyte migration, and inflammatory responses.

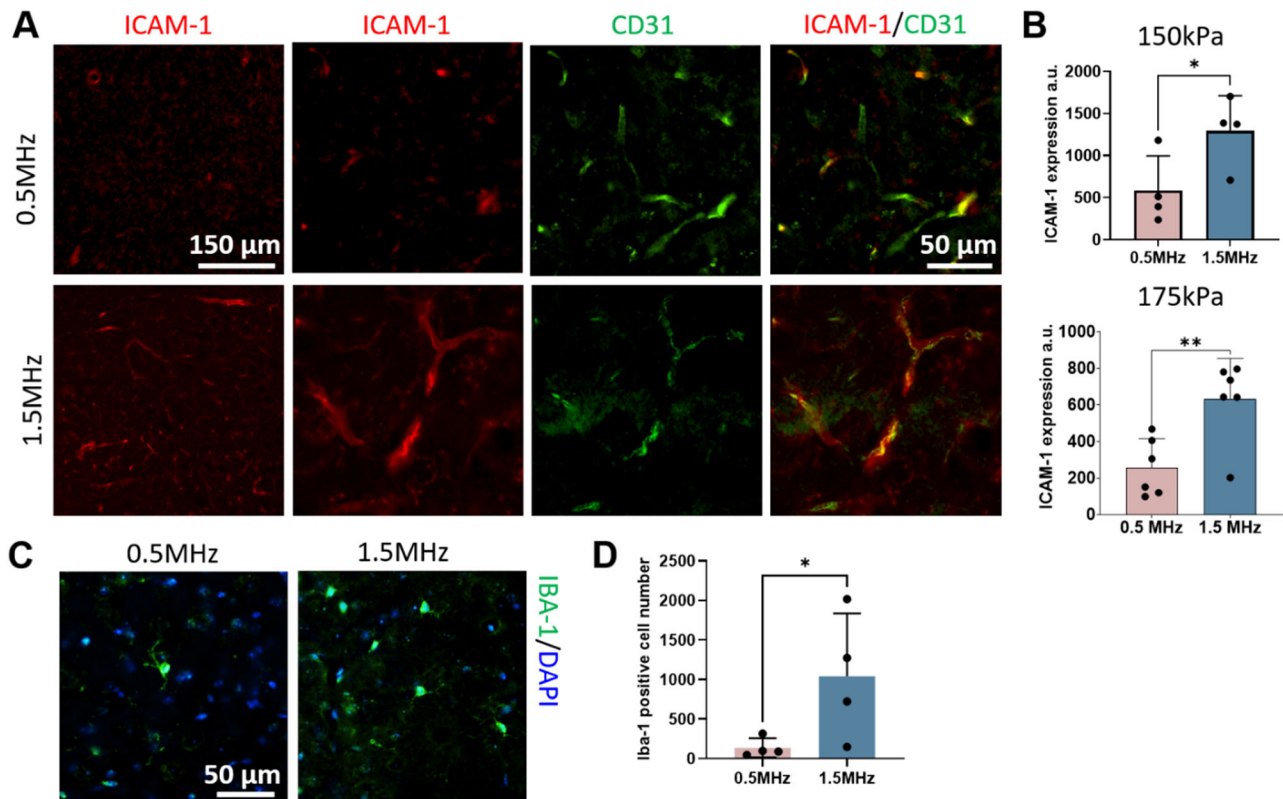


Fig. 5 | Protein expression analysis in mouse brain tissue. **A** Representative fluorescent microscopy data of ICAM-1 expression at 8 h after MB-FUS treated with 150 kPa. Red, ICAM-1; green, CD31. **B** Quantification of ICAM-1 expression treated with 150 kPa (upper) and 175 kPa (lower) pressure ($n = 4$ for 150 kPa group, $n = 6$ for 175 kPa group) ($p = 0.011$ for 150 kPa group, $p = 0.006$ for 175 kPa group).

C Representative fluorescent microscopy data of IBA-1 expression at 8 h after MB-FUS treated with 150 kPa. Green, IBA-1; blue, DAPI. **D** Quantification of IBA-1 expression treated with 150 kPa pressure ($n = 4$, $p = 0.049$). Measurements were taken from distinct samples. Plots show means \pm SD. *P*-values were determined by two-tailed paired *t* tests. * $P \leq 0.05$, ** $P \leq 0.01$.

inflammatory activity observed in the higher frequency group (Fig. 5C, D).

In aggregate, our mathematical modeling and experimental investigations revealed a previously unknown role of US frequency in promoting differential gene expression in BBB ECs and supported our hypothesis that MB resonant effects can be employed to elicit distinct transcriptional and functional changes in the BBB. Interestingly and contrary to current evidence, these responses do not correlate with changes in the BBB permeability, as assessed by DCE-MRI (i.e., K^{trans} values), indicating that it is possible to attenuate the inflammatory responses while opening the BBB.

US frequency can modulate CAR-T cell trafficking in SB28 Glioma tumors

In light of the above findings and the potential of MB resonant effects in brain vessels to regulate the expression of molecules that play a critical role in mediating T cell trafficking across the BBB^{63–65}, we

hypothesized that US frequency-tuned MB dynamics can impact the trafficking of cytotoxic T cells in brain tumors (Fig. 6A). To test our hypothesis, we focused on glioblastoma (GBM), as it is a lethal tumor with no effective treatments⁶⁶, and it is the focus of both FUS interventions^{15,67} and emerging immunotherapeutic approaches based on CAR-T cells⁶⁸. We employed the orthotopic SB28-EGFRvIII glioma model, as epidermal growth factor receptor variant III (EGFRvIII) is a human GBM-specific antigen⁶⁹. Furthermore, the SB28 glioma cell line is poorly immunogenic and grows in syngeneic C57BL/6 mice⁷⁰. To assess the impact of US frequency on CAR-T cell trafficking in the SB28-EGFRvIII glioma model (Fig. 6A), we employed a fully murinized version of the anti-EGFRvIII CAR-T cells⁷¹. To minimize differences in the BBB permeability and other tumor microenvironmental factors across different animals that can be influenced by tumor size, mice were distributed equally between groups based on tumor size, as indicated by MRI (Fig. 6B). Following systemic administration of the CAR-T cells, we administrated 2 μm lipid MB and sonicated 4–5 nonoverlapping

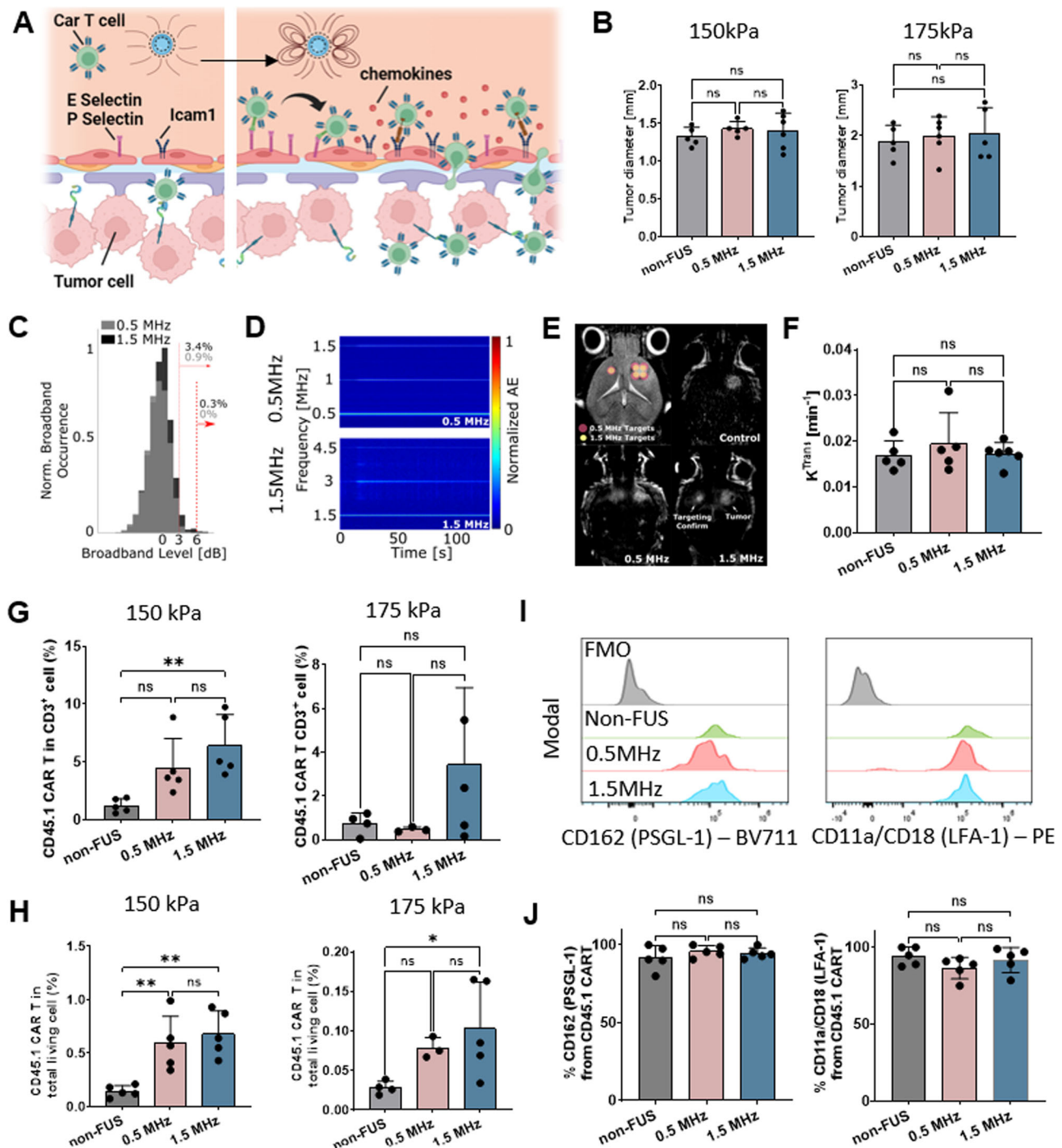


Fig. 6 | Enhanced infiltration of epidermal growth factor receptor variant III (EGFRvIII) CAR-T cells in SB28 Glioma tumor model after sonication with 1.5 MHz frequency. **A** Schematic illustration of CAR-T cells infiltration to brain tumor with MB-FUS using different ultrasound frequencies. Schematic created with BioRender.com. **B** Group assignment before treatment based on the quantification of tumor size for 150 kPa (left) and 175 kPa (right) pressure ($n = 5$). **C** Broadband emission (> 3 dB) probability during MB-FUS sonication using 175 kPa. **D** Spectrogram during sonication using 175 kPa pressure. Harmonic levels increased significantly following microbubble arrival to the brain, after a bolus injection at $t = 10$ s. Color bar normalized acoustic emission. **E** Representative T1-weighted MR images for healthy targets and targets in the tumor region. **F** Quantification of K^{Trans} value in tumor for 0.5 MHz and 1.5 MHz frequency treated with 175 kPa ($n = 5$). **G** Quantification of the percentage of CAR T cells in CD3 positive cells in SB28 glioma tumor when treated with 150 kPa (left, $n = 5$) and

175 kPa (right, $n = 4$ for non-FUS and 0.5 MHz group, $n = 5$ for 1.5 MHz group). (non-FUS vs 1.5 MHz (150kPa), $p = 0.006$). **H** Quantification of the percentage of CAR T cells in all live cells in SB28 glioma tumor when treated with 150 kPa (left, $n = 5$) and 175 kPa (right, $n = 4$ for non-FUS and 0.5 MHz group, $n = 5$ for 1.5 MHz group) (150 kPa: non-FUS vs 0.5 MHz, $p = 0.009$; non-FUS vs 1.5 MHz, $p = 0.002$; 175 kPa: non-FUS vs 1.5 MHz, $p = 0.049$). **I** Representative flow cytometry diagrams for receptors on SB28 tumor-infiltrating CAR T cells, PSGL-1 (left) and LFA-1 (right) when treated with 150 kPa. **J** Quantification of the percentage of the infiltrated CAR-T cells expressing PSGL-1 (left) and LFA-1 (right) when treated with 150 kPa. Measurements were taken from distinct samples. Plots show means \pm SD ($n = 5$). P -values were determined by one-way analysis of variance (ANOVA) and were adjusted using Bonferroni correction. n.s. no significance $P > 0.05$, $*P \leq 0.05$, $**P \leq 0.01$.

regions to cover the whole tumor with 0.5 MHz and 1.5 MHz frequency at 150 kPa and 175 kPa peak negative pressures for each frequency. The acoustic emission signal indicated strong harmonic emissions, while broadband emissions of less than 3 dB were present in less than 0.5% and 1% of the sonications for 150 kPa and 175 kPa, respectively (Fig. 6C, D). Following the sonication, we assessed the BBB permeability using DCE-MRI, which showed no difference among the 3 groups, non-FUS control, 0.5 MHz, and 1.5 MHz groups, indicating that the sonications did not increase further the tumor-induced dysregulated BBB permeability, as evidenced by DCE-MRI (Fig. 6E, F and Supplementary Fig. 13). Subsequently, we assessed the infiltration of EGFRvIII CAR-T cells to the SB28-EGFRvIII tumor microenvironment 48 h after sonication using flow cytometry analysis. Using a range of metrics (Fig. 6G, H), the CAR T cell infiltration at the high-frequency group is significantly higher than that of the control group at both pressures. For the low-frequency group, the differences in CAR T cell trafficking as compared to control are significant for some metrics and not for others. While we were unable to identify significant differences between the low and high-frequency groups, as evidenced by our data, high frequency leads to more robust responses (Fig. 6G, H). Crucially, our data also revealed that over 86% of the tumor-infiltrating CAR-T cells express PSGL-1 and LFA-1 receptors that interact with P-selectin and ICAM-1 cell adhesion molecules and play a key role in the process of leukocyte extravasation^{63,72–74} (Fig. 6I, J). Together, these findings demonstrate that tuning the US frequency can improve CAR-T cell trafficking, potentially through upregulation of cell adhesion molecules in the glioma tumor microenvironment. They are also consistent with current evidence that indicates CAR-T cells have limited accumulation in brain tumors despite having leaky BBB⁷⁵ and further support the functional relevance and potential clinical significance of the observed immuno-mechano-biological changes.

Discussion

In this work, we demonstrated that US frequency can be tuned to elicit distinct immuno-mechano-biological effects on BBB signaling and function. Our findings that critically expanded past observations that hinted at the possibility of promoting differential gene expression under specific MB properties⁷⁶ also support the notion that MB resonant effects can play a key role in the observed changes in BBB signaling and function. Perhaps the most salient finding of our investigations is that the BBB permeability and the expression of key inflammatory markers are not monotonically linked. This is contrary to current understanding²⁸. This discovery provides a better definition of the treatment window of current targeted drug delivery strategies, as it will allow to maximize therapeutic outcomes, while balancing safety concerns associated with acute inflammation²⁸. The latter is particularly important when multiple treatments (i.e., sonications) are needed due to dose (i.e., drug) limiting considerations^{12,13}. For this purpose, MBs with more elastic shells that are excited at frequencies below their resonance are preferred as they can prevent excessive inflammatory responses without lowering the BBB permeability, which is critical for improved drug delivery. This approach may also be beneficial for diagnostic interventions, such as US-enhanced liquid biopsy^{77,78}, where attaining high BBB permeability while suppressing inflammation will improve the safety profile of this diagnostic intervention. It is also important to note that while we did not observe any differences in the BBB permeability between the two frequencies, it is possible they may have impacted the BBB permeability in a way that the relatively small molecular weight (558.7 Da) MRI contrast agent we employed was not able to capture. Further investigations to assess the amplitude and duration of the BBB permeability at different excitation frequencies and for different molecules are warranted.

Interestingly, the transcriptional analysis of ECs revealed that certain genes are more responsive to MB-FUS at the lower pressure of 150 kPa compared to 175 kPa, though not all differences are statistically

significant (Fig. 4D, E and Supplementary Fig. 12). This trend in transcript changes agreed with the acoustic emission data, which showed higher harmonics level at 150 kPa compared to 175 kPa at 1.5 MHz (Fig. 3 and Supplementary Figs. 15–17), albeit not significant. A possible explanation for this observation is that higher pressures may result in higher acoustic radiation force that may push the microbubbles closer to the vessel wall⁷⁹, which may dampen their oscillation and diminish their impact on the vessel wall. Moreover, at 175 kPa, we observed an increased ultra-harmonics and broadband signal, which is an indication that MB oscillation is at the inertial cavitation threshold, suggesting that at this level, the MBs might lose their sustained and symmetrical oscillation and exert lower stress on the wall⁸⁰. To gain more insights into this phenomenon, our modeling can be extended to incorporate these phenomena (radiation force and asymmetric MB oscillation). While for our modeling we employed microbubble parameters from the literature^{56,81–84}, it is possible that batch-to-batch and even vial to vial variability can lead to different microbubble properties. However, the agreement between the predictions of our mathematical model and in vivo experimental results indicates that this variability was not substantial. To increase precision, future studies should characterize the mechanical properties of the microbubbles (beyond their size) prior to each experiment.

To explore if our findings from single microbubble oscillation are still valid when multiple microbubbles are present inside the vessel, we modeled two microbubbles inside the vessel. While our current implementation does not account for bubble-bubble interaction (e.g., microbubble coalescence), it demonstrates that for microbubble distances down to 3 μm , the frequency-dependent trend of microbubble oscillation and WSS remain consistent with the findings for the single microbubble, despite the differences in the microstreaming pattern in the surrounding fluid. Experiments examining the flow field around multiple oscillating microbubbles indicate that groups of three and four microbubbles in symmetrical arrangements exhibit similar flow behavior to the two-bubble cases, suggesting that the findings from our two-bubble model can also be applied to multi-bubble scenarios³³. Finally, improving the current high frame rate optical methods to provide direct visualization of the MB dynamics inside brain vessels can be used to further refine our understanding of the impact of MB-mediated mechanical stress on neurovascular mechanobiology.

Based on the transcriptional analysis suggesting that MB resonant effects in brain vessels can regulate inflammatory responses, we hypothesized that US frequency-tuned MB dynamics could impact the trafficking of cytotoxic T cells in brain tumors. Our findings indicate that the high-frequency sonication (i.e., above resonance) leads to a robust improvement in CAR T cell trafficking (Fig. 6). We also observed that over 86% of the tumor-infiltrating CAR-T cells express PSGL-1 and LFA-1 receptors, which interact with P-selectin and ICAM-1 (Fig. 6). This is critical as the upregulation of P-selectin on endothelial cells that can be triggered by inflammation facilitates T cell rolling through the interaction between PSGL-1 on T cells^{72,73}. Moreover, following this rolling process, ICAM-1 acts as an anchor for integrins such as LFA-1, firmly arresting T cells to the endothelium, which is a prerequisite for initiating paracellular diapedesis (extravasation)^{63,74}. These cell adhesion molecules were highly upregulated, as evidenced by the RNAseq data and immunostaining of the protein expression (ICAM-1) (Figs. 4D, 5A, B). While we cannot exclude the involvement of other pathways, future studies involving the knockdown of ICAM-1 can further consolidate our findings and provide additional mechanistic insights on the potential of US frequency and microbubble resonant effects to facilitate therapy (e.g., improve CAR-T cell trafficking in brain tumors).

Together, these findings not only corroborate recent investigations that alluded to the abilities of MB-FUS to increase CAR-T cell delivery in brain tumors^{17,19} but also provide critical insights on the role

of US frequency and MB resonant effects in augmenting cytotoxic immune cell trafficking in brain tumor microenvironment. Note that this is a significant challenge in brain cancer immunotherapy, where the BBB is considered a rate-limiting factor to the systemic delivery of cytotoxic T cells, such as CAR-T cells⁷⁵. While the BBB can be bypassed by direct infusion of CAR-T cells in brain tumors, these approaches offer only short-term benefits, since they cannot affect distant tumor cell infiltrations, as evidenced by tumor relapse^{85,86}. Beyond facilitating immune cell trafficking, the ability to tune the BBB signaling may also support the development and refinement of nanotherapeutic strategies that rely on the upregulation of specific BBB signaling pathways, such as p-selectin, for delivering their cargo in the brain^{87,88}.

While the above extensions will provide additional insights on the MB dynamics and interactions with the BBB, our investigations provide critical foundational knowledge towards understanding the impact of US frequency and MB properties on brain vasculature and reveal their abilities to elicit differential gene expression in the BBB, thereby creating new opportunities for safer and more effective diagnostic and therapeutic interventions across a range of brain diseases, including Alzheimer’s^{12,13}. Finally, the conceptual contributions of our research may also motivate therapeutic and diagnostic interventions outside of the brain, where the insights gained about the interaction of MB dynamics with vessels are both relevant and unexplored.

Methods

In vivo experiments

All animal procedures were performed according to the guidelines of the Public Health Policy on the Humane Care of Laboratory Animals and approved by the Institutional Animal Care and Use Committee of Georgia Institute of Technology. 8–0 weeks old female C57BL/6J mice (Jackson Laboratory) were used in this study.

Mathematical modeling of microbubble dynamics

To understand the transport dynamics of the ultrasound-microbubble-brain system, we developed a mathematical model that captures the acoustically driven MB dynamics inside a vessel and its interaction with surrounding fluid along with the fluid transport across the vessel wall and in the interstitial space. The MB dynamics, when it interacts with the ultrasound field in the unbounded fluid, acts as a resonant system and can be modeled as a mass-spring system where the gas core can be considered a spring, fluid is the mass, and ultrasound wave is the driving force. The microbubble oscillation can be described reasonably well by a modified Rayleigh-Plesset (RP) equation that accounts for the effect of MB shell, which is a major source of damping of bubble dynamics⁸⁹, as follows:

$$\rho \left(R\ddot{R} + \frac{3}{2}\dot{R}^2 \right) = \left[P_0 + \frac{2\sigma(R_0)}{R_0} \right] \left(\frac{R_0}{R} \right)^{3\kappa} - \frac{2\sigma(R)}{R} - 4\mu \frac{\dot{R}}{R} - 4\kappa_s \frac{\dot{R}}{R^2} + P_{ac}(t) - P_0 \quad (1)$$

R is the MB radius, ρ is the density of the surrounding fluid, P_0 is the ambient pressure, κ is the polytropic gas constant, μ is the fluid viscosity, κ_s is the shell surface viscosity. The acoustic pressure, $P_{ac}(t) = A \sin \omega t$, is considered a continuous sinusoidal wave, where A is the amplitude of acoustic pressure, and ω is the angular frequency of the acoustic wave. The acoustic pressure was assumed to be uniform around the bubble as the wavelength of the ultrasound wave is much larger than the MB size. This equation is modified further to capture the non-linear effect of bubble oscillation by separating the shell motion into three regimes (buckled, elastic, and ruptured region) as suggested by Marmottant et al.⁵⁴. This modification is described by the change of surface tension, σ , during bubble expansion and at shell

break-up as follows:

$$\sigma(R) = \begin{cases} 0, & \text{if } R < R_{buckling} \\ \chi \left(\frac{R^2}{R_{buckling}^2} - 1 \right), & \text{if } R_{buckling} < R < R_{break-up} \\ \sigma_{water}, & \text{if } R > R_{ruptured} \end{cases} \quad (2)$$

where χ is the shell elastic modulus, $R_{buckling}$ is the MB radius at which the shell buckles and is assumed to be the MB resting radius, and $R_{ruptured} = R_{buckling} \sqrt{\left(\frac{\sigma_{water}}{\chi} \right) + 1}$ is the MB radius when MB shell rupture⁵⁴.

To study the interaction of MB with the vessel wall and surrounding fluid, the MB model was incorporated into a finite element model. The model consists of a luminal area, vascular wall, and interstitial space. The MB was placed in the center of the vessel with a radius of 5–10 μm and a thickness of 1 μm . For the interaction between MB and surrounding fluid, MB dynamics is coupled with the fluid dynamics inside the vessel, which was modeled by assigning a pressure boundary condition, P_b , at the MB-fluid interface, shown in Eq. (3)^{90,91}. The fluid dynamics inside the vessel are modeled using the Navier-Stokes equation assuming incompressible and Newtonian fluid.

$$P_b = \left[P_0 + \frac{2\sigma(R_0)}{R_0} \right] \left(\frac{R_0}{R} \right)^{3\kappa} - \frac{2\sigma(R)}{R} - 4\mu \frac{\dot{R}}{R} - 4\kappa_s \frac{\dot{R}}{R^2} + P_{ac}(t) - P_0 \quad (3)$$

To confirm the finite element modeling of MB dynamics was implemented correctly, the MB dynamics of in an unbounded fluid field is compared with RP solution solved by ODE solver (Supplementary Fig. 1A, B).

Then, the microbubble dynamics in a confined vessel were considered. The vessel wall and interstitial space were considered as porous material and the fluid flow was modeled with Brinkman equation⁹¹. Zero pressure boundary conditions are applied to the boundaries of the computational domain, which is 100 times larger than the size of MB both in height and width. To study the forces exerted by microbubble oscillation on the vessel wall, we calculated the shear stress (τ_{rz}) on the vessel wall as follows:

$$\tau_{rz} = \mu \left[\frac{du}{dz} + \frac{dw}{dr} \right] \quad (4)$$

where r and z are radial and axial components of cylindrical coordinate, μ is the fluid viscosity, and u and w are fluid velocity components in the r and z direction, respectively.

The whole domain was discretized using triangular elements with refined mesh at the MB boundary and the vascular wall (average mesh edge length 0.005 μm along the MB surface and 0.2 μm along the vascular wall). The arbitrary Lagrangian-Eulerian method (ALE) was used for the mesh movement at the MB boundary and luminal domain. To study the MB dynamics under real experimental conditions, we used the focal pressure that was used in our experiment (150 kPa and 175 kPa) at the MB surface in our model⁹². The parameters used in this mathematical model are summarized in Supplementary Table 1. The simulations were performed using the commercial finite element software, COMSOL (version 5.5, Burlington, MA, USA), where necessary equations were added using the Mathematics module.

Using this model, to assess the relative importance of parameters, including MB shell viscosity, MB shell elasticity, fluid viscosity, and vessel wall porosity, on the WSS, we performed a parametric sensitivity analysis. Specifically, we varied (one at a time) the modeling parameters (P_j) and calculate the resulting impact on the WSS by using the equation $Sensitivity = \text{avg}(P_j) \frac{\Delta WSS}{\Delta P_j}$.

To explore if the finding we got from single MB oscillation can also be applied to the case that multiple MB are present inside the vessel, we expanded our mathematical model to simulate the oscillation of two MBs inside the vessels with 5 μm apart between their center. The same pressure boundary condition, P_b , was applied at both MB-fluid interfaces.

Ultrasound guided focused ultrasound system

To perform the sonications and monitor the treatment in healthy mice, a custom-built portable USgFUS system was employed (Supplementary Fig. 2A). The system has high targeting accuracy (500 μm) and is capable of real-time monitoring of microbubble dynamics via passive cavitation detection (PCD). Firstly, the USgFUS system created a 2D contour of the mouse head, by raster scanning a single-element imaging transducer (3.5 MHz) mounted on a 3D-positioning system, which was used to determine the target locations with a reference of the eyes. The system was then allowed to perform sonication with a coaxial therapeutic FUS transducer operated at either the fundamental or third harmonic (0.5/1.5 MHz). The geometric focal distance, which was also confirmed by free field calibration, was 25 mm from the transducer surface. For BBB opening experiments, we followed the methods we have previously established and published¹⁶, where the transducer was precisely aligned using a pulse/echo scheme to guide transducer focus 3 mm below the skull. This also ensured acoustic coupling. Our ultrasound-guided FUS system (USgFUS) is submerged in the water tank, and the water tank is coupled with the animal head by fully covering the head with degassed ultrasound imaging gel (Aquasonic). The PCD is a 6 mm diameter planar single-element imaging transducer that is co-axially aligned with our FUS transducer. During sonication, the imaging transducer was switched to passive mode to capture MB's response (i.e., PCD) after high-pass filtering at 0.6 MHz/2 MHz cutoff frequencies with 20 dB gain, whose frequency spectrum was then normalized to the mean of spectrum recorded before MB arrival to remove unnecessary emissions other than MB response. Microbubbles, during stable or inertial volumetric oscillations, radiate diverging spherical pressure waves (acoustic emissions). Stable oscillations radiate harmonic, ultra-, and sub-harmonic emissions of the excitation frequency. MB collapse (i.e., inertial cavitation) is accompanied by broadband emissions. Hence the analysis of the recorded acoustic emissions through PCD during the sonication can be used to characterize the type of MB oscillations. Specifically, these data allow first to confirm that the observed effects are not related to MB collapse and second to indirectly assess the strength of the oscillations (i.e., stronger oscillations will lead to stronger emissions). Harmonic, ultra-harmonic, and broadband levels were obtained by taking the mean of ± 5 frequency bins from each harmonic frequency $-6f_0$, $6.5f_0$, and $7.22f_0$ for 0.5 MHz and $3f_0$, $2.5f_0$, and $2.22f_0$ for 1.5 MHz, respectively, which were selected considering the center frequency of PCD (3.5 MHz).

Calibration of the focused ultrasound transducer

The focused ultrasound transducer's (fundamental and third-harmonic 0.5 MHz and 1.5 MHz, respectively; Sonic Concepts) pressure was calibrated both in free-field and transcranial conditions. For accurate comparison between the trans-skull pressure between 0.5 and 1.5 MHz, transcranial focal pressure was used throughout the study. Free field pressures for each frequency were obtained by voltage sweep after aligning 2 mm needle hydrophone (Precision Acoustics; NH2000 - SN 3515, Preamplifier - SN HP33385) to the focus of transducer. In addition, for each frequency, the transcranial focal pressure was obtained similar to the free field (by locating the focus using a hydrophone and 3D positioning system), but after placing a mouse skull in between the transducer and hydrophone. The vertical position of the skull was carefully adjusted using pulse/echo so that the geometric focus of the transducer was at ~ 4 mm inside the skull

structure; the lateral position of the skull was also adjusted to a similar location used in our health in vivo studies and tumor injection sites. At each frequency and condition, 30 cycle pulse was used, and the maximum peak-to-peak pressures were used to obtain the calibration curve (Supplementary Fig. 4A). Here, to account for double-reflection, we used the maximum pressure just before the reflected wave's constructive interference started to occur. The attenuation and absorption from obstacles other than the skull were assumed similar to water. The resulting calibration was further validated through simulation to confirm the absence of standing waves and to assess how our experimental calibration would be affected when applied in vivo (Supplementary Fig. 4).

COMSOL simulation of transcranial focused ultrasound

To test whether our results from the transcranial pressure calibration were significantly changed in vivo conditions, we first simulated the pressure field through a skull fraction (obtained from a CT image) to mimic our transcranial pressure calibration method (i.e., the alignment geometry). Then, we selected transducer surface pressures that resulted in the same focal pressure for each frequency (0.5 and 1.5 MHz) through the skull fraction. Using these surface pressures, we simulated the pressure field through a full skull with brain and air cavity (mouth and airway) incorporated (Supplementary Fig. 4 B), at the same location. Using mouse skull and medium properties from past publications⁹³⁻⁹⁵, we found approximately 5% (for 0.5 MHz) and 20% (for 1.5 MHz) more attenuated pressure after applying a full skull with air cavity at the bottom, compared to skull fraction-only simulation.

Microbubble preparation and characterization

The MBs used in this study were the clinical grade commercial MBs, Definity, and Optison, which have polydisperse size distribution. To independently access the effect of MB parameters on the vessel, we isolated the MBs into different sizes using buoyancy force. Definity MBs were separated into two different sizes, $0.86 \mu\text{m} \pm 0.1 \mu\text{m}$ and $1.9 \mu\text{m} \pm 0.05 \mu\text{m}$ in diameter, respectively. For Optison, MBs with a diameter of $1.92 \mu\text{m} \pm 0.12 \mu\text{m}$ were selected. To make sure the MB sizes and number of MBs selected were consistent using this method, the selected MB were characterized by Multisizer 4e (Beckman Colter, CA, USA), Zetasizer Nano (Malvern Instrument, Malvern, UK) and confirmed using optical microscopy (60x magnification).

Focused ultrasound treatment procedure

For the MB-FUS experiments, the following exposure settings were employed: 10 msec bursts, pulse repetition frequency of 2 Hz, for a total treatment time of 2 min with concurrent intravenous (i.v.) tail vein administration of MB (Optison/Definity, 1×10^7 MB/sonication). MBs were administered using infusion for the experiments comparing Optison and Definity MBs to make sure the MB concentration was constant throughout the sonication and to account for the different clearance times of these two MBs. Bolus administration was used for all other experiments. If multiple sonications were performed in the brain of the same mouse, we waited at least 5 min before starting the next sonication to ensure that the injected MB was completely cleared from the body (Supplementary Fig. 2 B). Immediately after the sonication, the animals were injected with a gadolinium contrast agent, and changes in BBB permeability were assessed using Dynamic Contrast-Enhanced Magnetic Resonance Imaging (DCE-MRI). Finally, the brains were harvested for further processing after performing transcardial perfusion with sterile ice-cold PBS.

Magnetic resonance imaging

To access the vessel permeability in the brain (assuming that tissue perfusion was the same across samples), the volume transfer constant, K^{trans} , which provides a measure that combined effects of vascular

permeability, blood flow, and capillary surface area, was measured by performing DCE-MRI (IR, echo time, 2.5 ms; rep time, 30 ms; FOV, 20 × 20 mm²; flip angle, [2°, 5°, 10°, 15°, 20°, 30°]). More specifically, the DCE-MRI was acquired with concurrent bolus administration of 8 µl gadolinium contrast agent (279.3 mg/ml, ProHance). The collected DCE-MRIs datasets were analyzed, and K^{trans} values were calculated in Horos using the DCE tool plugin (Kyung Sung, Los Angeles, California). To cover the whole MB-FUS treated region, three coronal slices with 1 mm thickness were imaged, and the maximum K^{trans} value of the three imaged slices was used to compare across the experimental groups (Figs. 1H, 2E, F, 3I, 5E, F). The mean and median of the K^{trans} values were also calculated in Supplementary Figs. 5, 12. The arterial input function (AIF) was obtained based on the method developed by Fritz-Hansen et al.⁹⁶, as provided in the DCE tool plugin.

Bulk RNA sequencing of brain endothelial cells

Immediately after euthanasia with transcatheter perfusion with sterile ice-cold PBS (8 h and 24 h after treatment), the mouse brains were harvested. The front quadrants (FUS-treated region) were collected and then dissociated using Neural Tissue Dissociation Kits (P) (Miltenyi Biotec, Cat#A130-092-628), followed by cell debris removal using Debris removal solution (Miltenyi Biotec, Cat#130-109-398). Next, to isolate endothelial cells from all cell populations, we labeled Pecam-1 positive cell with a magnetic bead (Miltenyi Biotec, Cat# 130-097-418) and passed the cell through a magnetic separator. Finally, RNA extraction was performed using the RNeasy Mini Kit (Qiagen).

The quality of the extracted RNA, an average RIN number of 8.5 ± 0.98 was determined using an Agilent Bioanalyzer 2100. mRNA was then isolated using the NEBNext Poly(A) mRNA isolation module and libraries were prepared using the NEBNext Ultra II directional RNA library preparation kit. The libraries were then sequenced on an Illumina NextSeq 500 and an Illumina NovaSeq 6000 at a target depth of ~30 million PE100bp reads per sample.

Bulk RNA sequencing analysis

We used the *Rsubread* R package to generate a genome index using the mm10 version of the mouse genome for read alignment. The fastq files containing the reads from sequencing were then aligned to the generated mouse genome index, and BAM files were generated as outputs. Reads that were mapped were quantified for each gene, followed by conversion into a DGEList object with the *edgeR* R package. Furthermore, we annotated the genes using the *org.Mm.eg.db* R package. For quality control, only the genes with a count-per-million (CPM) value greater than 0.4 in at least 2 out of 58 sample libraries were kept, which filtered out the genes with a low read count. The normalization factor was calculated for each sample, and 3 matrices were generated for post-processing from the DGEList object: count matrix with read counts for each gene for each sample, gene matrix with gene names, and normalization matrix with normalization factors for each sample.

The gene names were converted from Entrez Gene ID to Gene Symbol with the gene matrix, while the count matrix was normalized with the normalization matrix. Counts of the replicates from the same experimental groups were averaged, and fold changes were computed using the average values of two different groups. *P*-values were calculated for comparison of these two groups using the T.TEST function in Excel with assumptions of a two-tailed distribution and two samples of unequal variance. Log base 2 of fold change (log₂FC) and -log base 10 of the *p*-value (log₁₀pval) were $\text{com}0.58$ ($\text{FC} = +/ - 1.5$) and $-\log_{10}pval = 1.3$ ($p\text{-value} = 0.05$) were set as thresholds for significant changes of genes. To identify the enriched biological processes, we performed Gene Ontology enrichment analysis^{97,98} using PANTHER on the selected 200 genes in each MB-FUS treated group that were significantly upregulated/downregulated and had the highest fold change as compared to the non-FUS control group. In addition, we generated

heatmaps of the z score of lists of genes that are associated with mechanical forces stimuli, leukocyte migration, and inflammatory responses based on the Gene Ontology enrichment analysis.

Immunofluorescence staining and microscopy

For protein expression analysis, after the animals were euthanized at the time point based on their treatment protocols (1 h or 6 h after MB-FUS), the brains were harvested and were fixed with 4% PFA overnight at 4 °C followed by 30% sucrose solution (4 °C) until it sunk to the bottom of the container. The brains were placed in an O.C.T. compound and rapidly froze to -80 °C. Subsequently, 20 µm sections were cut using a cryostat (Leica 3050 S Cryostat).

To assess the biological effect induced by MB-FUS, immunofluorescence staining was performed on the brain tissue. Tissues were prepared for staining by fixing in 4% paraformaldehyde at room temperature for 10 min (For sections requiring staining of intracellular markers (e.g., Iba-1), they were permeabilized with 0.1% Triton X-100 in PBS for 5 min, subsequently). After washed with PBS, the sections were blocked for 1 h at room temperature (2% Bovine Serum Albumin, 5% goat serum in PBS). It was then incubated with primary antibody diluted in 1% Bovine Serum Albumin (1:100) for 12 h at 4 °C. CD31 antibody (Invitrogen 14-0311-85) was used to stain endothelial cells. Claudin-5 Monoclonal Antibody (35-2500, Invitrogen) was used for tight junction protein staining, and CD54 ICAM-1 Monoclonal Antibody (14-0542, Invitrogen) was used for the staining of the inflammatory marker. In addition, the anti-Iba1 antibody (ab178846, Abcam) was used for the staining of Iba1. Next, the sections were incubated with a secondary antibody diluted in 1% Bovine Serum Albumin (1:250) for 1 h at room temperature. To stain the cell nucleus, samples were incubated with DAPI diluted in PBS (1:1000, 62248, Invitrogen) for 10 min after washing. Finally, the sections were rinsed with PBS to remove excess antibodies, mounted with mounting medium (Prolong Glass Antifade Mountant, Lot# 2018752, Invitrogen), and covered with coverslips. Samples were cured with a mounting medium for 24 h in the dark at room temperature before imaging.

The sections were imaged with a 20x objective using a fluorescence microscope (Eclipse Ti2, Nikon). The excitation wavelengths used for the cell nucleus, ICAM-1/Claudin-5, were 405 nm and 639 nm, respectively. The quantification of the fluorescence images was performed using ImageJ. To quantify ICAM expression, we used the CD31 staining as a mask and quantified the ICAM intensity only for the areas that were colocalized with CD31 positive staining. Similar to IBA-1 quantification, we counted the IBA-1 positive cells intensity only if they were colocalized with DAPI staining.

Immunohistochemistry staining

Hematoxylin-eosin staining was performed to examine tissue damage and safety. 20 µm thick frozen sections (Leica 3050 S Cryostat) were dehydrated beforehand and stained using a Leica Autostainer (ST5010). The sections were imaged with a 20x objective using a brightfield microscope (Eclipse Ti2, Nikon).

SB28 glioma cells and tumor inoculation

The murine glioma cell line SB28, which was retrovirally transduced with human EGFRvIII, was provided by Dr. Hideho Okada's lab at the University of California San Francisco. A detailed description of the cell line is available in a previous study⁷¹. SB28 glioma cells were cultured in complete RPMI [cRPMI: RPMI 1640 media with 10% FBS, 1% Penicillin-Streptomycin (Gibco, 15070063), 1% HEPES (Gibco, 15630080), 1% Glutamax (Gibco, 35050061), 1% non-essential amino acids (Gibco, 11140076), 1% sodium pyruvate (Gibco, 11360070), 0.5 mM 2-Mercaptoethanol (Gibco, 21985023)] media containing 10 µg/µl puromycin.

SB28 glioma cells (2×10^4 cells) were stereotactically implanted into the brain at 1 mm anterior, 1 mm to the right, and 3 mm deep of the

bregma of 6- to 8-week-old female C57BL/6J mice (The Jackson Laboratory). After cell implantation, tumor growth was monitored using T2-weighted MRI (echo time = 35 ms, repetition time = 2.5 s, rapid acquisition with refocusing echos factor = 8, slice thickness = 1 mm), and MB-FUS treatments were performed when tumors reached a size of ~20–40 mm³ after 9–11 days of tumor inoculation. To minimize differences related to tumor size, before each experiment, the tumors in all animals were measured with MRI and spread equally between treatment groups. The animals were considered as their endpoint if they exhibited severely impaired activity, significant weight loss, tumor dimensions exceeding 20 mm, or if treatment-related severe adverse events occurred that caused pain or distress and that could not be ameliorated. None of the tumors met the endpoint criteria throughout the study.

EGFRVIII CAR-T cells delivery in the glioma tumor model with MB-FUS

The EGFRVIII-specific CAR-T cells were also provided by Dr. Hideho Okada's lab at the University of California San Francisco. These CAR-T cells were derived from the EGFRVIII-CAR transgenic mouse strain and prepared as we reported in a previous study⁷¹.

Mice received lymphodepletion 18–20 h prior to systemic adoptive cell therapy with a combination of cyclophosphamide (4 mg/mouse) and fludarabine (1 mg/mouse) administered through intraperitoneal injection (i.p.). More specifically, cyclophosphamide (Baxter, NDC 10019-955-01) was resuspended in sterile saline at 40 mg/ml immediately prior to use, and 4 mg per mouse was administered by i.p. injection. Fludarabine phosphate (Sagent, NDC 25021-242-02, 25 mg/ml) was stored at 4 °C, and 1 mg per mouse was administered by i.p. injection.

For the trafficking experiments, mice bearing SB28-EGFRVIII⁺ gliomas received systemic adoptive cell therapy in combination with MB-FUS treatment. A single intravenous (i.v.) tail vein infusion of EGFRVIII CAR-T cells (2.5×10^6 cells) was performed 30 min before the application of MB-FUS.

Isolation of tumor-infiltrating leukocytes and flow cytometry

To assess CAR-T cell infiltration into the tumor, we performed flow cytometry. Forty-eight hours after treatment, mice were euthanized and then immediately received intracardiac perfusion of 10 mL sterile PBS. The whole brain was dissected, and the entire tumor mass was separated from the brain. Tumors were immediately minced with sterile scalpels. Tumor fragments were washed with PBS and enzymatically digested with a cocktail of collagenase IV (Worthington, 3.2 mg/mL) and deoxyribonuclease I (Worthington, 1 mg/mL) diluted in sterile PBS at 37 °C for 45 min. After digestion, cells were filtered through a 70 µm cell strainer, washed with sterile PBS, and resuspended in a 70% Percoll (Cytiva) solution. The suspensions were overlaid with 30% Percoll and HBSS and then centrifuged for 30 min at 650 g. Enriched tumor-infiltrating leukocyte (TIL) populations were recovered at the 70% to 30% Percoll interface.

Single-cell suspensions (0.5×10^6 cells) of tumor-infiltrating leukocytes (TILs) were pre-incubated with mouse FcR blocking solution containing anti-mouse CD16/32 antibody (BioLegend, 156604). After 10 min, a cocktail of fluorophore-conjugated antibodies resuspended in 50 µl of FC buffer (1X PBS, 0.5% FBS, 2 mM EDTA) was added directly to each tube, and samples were incubated at 4 °C for 20 min in the dark. Samples were washed with excess buffer and resuspended in FC buffer for analysis. CD45.1 was used as a detection marker for CAR-T cells (Biolegend 110743). CD3 CD45.2 cells were stained using the antibody Biolegend 100228 and Biolegend 109828, respectively. CAR T cell receptor LFA-1 and CD162 were stained using the antibodies Biolegend 141005 and Biolegend 148310, respectively. Zombie Aqua (Biolegend 423102) was used for live/dead cells staining. Samples were analyzed using a Cytex Aurora (Cytex) flow cytometer.

Statistical analysis

All statistical analyses were performed using GraphPad Prism. *P*-values $P < 0.05$ were considered statistically significant. (n.s. no significance, * $P \leq 0.05$, ** $P \leq 0.01$, *** $P \leq 0.0001$). In the case of multiple comparisons, the *p*-values were adjusted using Bonferroni correction.

Reporting summary

Further information on research design is available in the Nature Portfolio Reporting Summary linked to this article.

Data availability

All data supporting the findings of this study are available within the article and its supplementary files. Bulk RNA sequencing analysis is available at syn61969052 [<https://www.synapse.org/Synapse:syn61969052/wiki/629267>]. Any additional requests for information can be directed to and will be fulfilled by, the corresponding authors. Source data are provided in this paper. Source data are provided in this paper.

References

- Abbott, N. J. Blood–brain barrier structure and function and the challenges for CNS drug delivery. *J. Inherit. Metab. Dis.* **36**, 437–449 (2013).
- Vanlandewijck, M. et al. A molecular atlas of cell types and zonation in the brain vasculature. *Nature* **554**, 475–480 (2018).
- Wälchli, T. et al. Shaping the brain vasculature in development and disease in the single-cell era. *Nat. Rev. Neurosci.* 1–28. <https://doi.org/10.1038/s41583-023-00684-y> (2023).
- van Veluw, S. J. et al. Vasomotion as a driving force for paravascular clearance in the awake mouse brain. *Neuron* **105**, 549–561.e5 (2020).
- Kim, K. J., Diaz, J. R., Iddings, J. A. & Filosa, J. A. Vasculo-neuronal coupling: Retrograde vascular communication to brain neurons. *J. Neurosci.* **36**, 12624–12639 (2016).
- Hynynen, K., McDannold, N., Vykhotseva, N. & Jolesz, F. A. Non-invasive MR imaging-guided focal opening of the blood-brain barrier in rabbits. *Radiology* **220**, 640–646 (2001).
- Aryal, M., Arvanitis, C. D., Alexander, P. M. & McDannold, N. Ultrasound-mediated blood–brain barrier disruption for targeted drug delivery in the central nervous system. *Adv. Drug Deliv. Rev.* **72**, 94–109 (2014).
- Arvanitis, C. D. et al. Mechanisms of enhanced drug delivery in brain metastases with focused ultrasound-induced blood–tumor barrier disruption. *Proc. Natl. Acad. Sci. USA* **115**, E8717–E8726 (2018).
- Jordão, J. F. et al. Amyloid-β plaque reduction, endogenous antibody delivery and glial activation by brain-targeted, transcranial focused ultrasound. *Exp. Neurol.* **248**, 16–29 (2013).
- Poon, C., Pellow, C. & Hynynen, K. Neutrophil recruitment and leukocyte response following focused ultrasound and microbubble mediated blood-brain barrier treatments. *Theranostics* **11**, 1655–1671 (2021).
- Kovacs, Z. I. et al. Disrupting the blood-brain barrier by focused ultrasound induces sterile inflammation. *Proc. Natl. Acad. Sci. USA* **114**, E75–E84 (2017).
- Meng, Y., Hynynen, K. & Lipsman, N. Applications of focused ultrasound in the brain: from thermoablation to drug delivery. *Nat. Rev. Neurol.* **17**, 7–22 (2021).
- Leinenga, G., Langton, C., Nisbet, R. & Götz, J. Ultrasound treatment of neurological diseases — current and emerging applications. *Nat. Rev. Neurol.* **12**, 161–174 (2016).
- Schoen, S. et al. Towards controlled drug delivery in brain tumors with microbubble-enhanced focused ultrasound. *Adv. Drug Deliv. Rev.* **180**, 114043 (2022).

15. Anastasiadis, P. et al. Localized blood–brain barrier opening in infiltrating gliomas with MRI-guided acoustic emissions–controlled focused ultrasound. *PNAS* **118**, e2103280118 (2021).
16. Lee, H. et al. Spatially targeted brain cancer immunotherapy with closed-loop controlled focused ultrasound and immune check-point blockade. *Sci. Adv.* **8**, eadd2288 (2022).
17. Sabbagh, A. et al. Opening of the blood–brain barrier using low-intensity pulsed ultrasound enhances responses to immunotherapy in preclinical glioma models. *Clin. Cancer Res.* **27**, 4325–4337 (2021).
18. Sheybani, N. D. et al. ImmunoPET-informed sequence for focused ultrasound-targeted mCD47 blockade controls glioma. *J. Control. Release* **331**, 19–29 (2021).
19. Kim, C., Lim, M., Woodworth, G. F. & Arvanitis, C. D. The roles of thermal and mechanical stress in focused ultrasound-mediated immunomodulation and immunotherapy for central nervous system tumors. *J. Neurooncol.* **157**, 221–236 (2022).
20. Chen, K.-T. et al. Neuronavigation-guided focused ultrasound for transcranial blood-brain barrier opening and immunostimulation in brain tumors. *Sci. Adv.* **7**, eabd0772 (2021).
21. Han, S. et al. Tumour-infiltrating CD4+ and CD8+ lymphocytes as predictors of clinical outcome in glioma. *Br. J. Cancer* **110**, 2560–2568 (2014).
22. Leinenga, G. & Götz, J. Scanning ultrasound removes amyloid- β and restores memory in an Alzheimer’s disease mouse model. *Sci. Transl. Med.* **7**, 278ra33–278ra33 (2015).
23. Burgess, A. et al. Alzheimer disease in a mouse model: MR imaging-guided focused ultrasound targeted to the hippocampus opens the blood-brain barrier and improves pathologic abnormalities and behavior. *Radiology* **273**, 736–745 (2014).
24. Weber-Adrian, D. et al. Strategy to enhance transgene expression in proximity of amyloid plaques in a mouse model of Alzheimer’s disease. *Theranostics* **9**, 8127–8137 (2019).
25. Todd, N. et al. Secondary effects on brain physiology caused by focused ultrasound-mediated disruption of the blood–brain barrier. *J. Control. Release* **324**, 450–459 (2020).
26. Zhang, W., Xiao, D., Mao, Q. & Xia, H. Role of neuroinflammation in neurodegeneration development. *Sig Transduct. Target Ther.* **8**, 1–32 (2023).
27. Leng, F. & Edison, P. Neuroinflammation and microglial activation in Alzheimer disease: where do we go from here? *Nat. Rev. Neurol.* **17**, 157–172 (2021).
28. Kovacs, Z. I., Burks, S. R. & Frank, J. A. Focused ultrasound with microbubbles induces sterile inflammatory response proportional to the blood brain barrier opening: Attention to experimental conditions. *Theranostics* **8**, 2245–2248 (2018).
29. Stride, E. & Coussios, C. Nucleation, mapping and control of cavitation for drug delivery. *Nat. Rev. Phys.* **1**, 495–509 (2019).
30. McMahon, D. & Hynynen, K. Acute inflammatory response following increased blood-brain barrier permeability induced by focused ultrasound is dependent on microbubble dose. *Theranostics* **7**, 3989–4000 (2017).
31. Ji, R. et al. Cavitation-modulated inflammatory response following focused ultrasound blood-brain barrier opening. *J. Control. Release* **337**, 458–471 (2021).
32. McDannold, N., Arvanitis, C. D., Vykhodtseva, N. & Livingstone, M. S. Temporary disruption of the blood–brain barrier by use of ultrasound and microbubbles: Safety and efficacy evaluation in Rhesus Macaques. *Cancer Res* **72**, 3652–3663 (2012).
33. Tho, P., Manasseh, R. & Ooi, A. Cavitation microstreaming patterns in single and multiple bubble systems. *J. Fluid Mech.* **576**, 191 (2007).
34. Stride, E. & Saffari, N. Microbubble ultrasound contrast agents: A review. *Proc. Inst. Mech. Eng. H* **217**, 429–447 (2003).
35. Deprez, J., Lajoinie, G., Engelen, Y., De Smedt, S. C. & Lentacker, I. Opening doors with ultrasound and microbubbles: Beating biological barriers to promote drug delivery. *Adv. Drug Deliv. Rev.* **172**, 9–36 (2021).
36. Samiotaki, G., Vlachos, F., Tung, Y.-S. & Konofagou, E. E. A quantitative pressure and microbubble-size dependence study of focused ultrasound-induced blood-brain barrier opening reversibility in vivo using MRI. *Magn. Reson. Med.* **67**, 769–777 (2012).
37. Wang, S., Samiotaki, G., Olumolade, O., Feshitan, J. A. & Konofagou, E. E. Microbubble type and distribution dependence of focused ultrasound-induced blood–brain barrier opening. *Ultrasound Med. Biol.* **40**, 130–137 (2014).
38. Song, K.-H. et al. Microbubble gas volume: A unifying dose parameter in blood-brain barrier opening by focused ultrasound. *Theranostics* **7**, 144–152 (2017).
39. Vlachos, F., Tung, Y.-S. & Konofagou, E. Permeability dependence study of the focused ultrasound-induced blood–brain barrier opening at distinct pressures and microbubble diameters using DCE-MRI. *Magn. Reson. Med.* **66**, 821–830 (2011).
40. Choi, J. J. et al. Microbubble-size dependence of focused ultrasound-induced blood–brain barrier opening in Mice in vivo. *IEEE Trans. Biomed. Eng.* **57**, 145–154 (2010).
41. McDannold, N., Vykhodtseva, N. & Hynynen, K. Use of ultrasound pulses combined with Definity® for targeted blood-brain barrier disruption: a feasibility study. *Ultrasound Med. Biol.* **33**, 584–590 (2007).
42. Bing, C. et al. Characterization of different bubble formulations for blood-brain barrier opening using a focused ultrasound system with acoustic feedback control. *Sci. Rep.* **8**, 7986 (2018).
43. Dauba, A. et al. Recent advances on ultrasound contrast agents for blood-brain barrier opening with focused ultrasound. *Pharmaceutics* **12**, 1125 (2020).
44. Qin, S. & Ferrara, K. W. Acoustic response of compliant microvessels containing ultrasound contrast agents. *Phys. Med Biol.* **51**, 5065–5088 (2006).
45. Wiedemair, W., Tuković, Ž., Jasak, H., Poulikakos, D. & Kurtcuoglu, V. On ultrasound-induced microbubble oscillation in a capillary blood vessel and its implications for the blood–brain barrier. *Phys. Med. Biol.* **57**, 1019 (2012).
46. Hosseinkhah, N. & Hynynen, K. A three dimensional model of an ultrasound contrast agent gas bubble and its mechanical effects on microvessels. *Phys. Med Biol.* **57**, 785–808 (2012).
47. Chen, C., Gu, Y., Tu, J., Guo, X. & Zhang, D. Microbubble oscillating in a microvessel filled with viscous fluid: A finite element modeling study. *Ultrasonics* **66**, 54–64 (2016).
48. Hosseinkhah, N., Goertz, D. E. & Hynynen, K. Microbubbles and blood–brain barrier opening: A numerical Study on acoustic emissions and wall stress predictions. *IEEE Trans. Biomed. Eng.* **62**, 1293–1304 (2015).
49. Martynov, S., Stride, E. & Saffari, N. The natural frequencies of microbubble oscillation in elastic vessels. *J. Acoust. Soc. Am.* **126**, 2963–2972 (2009).
50. Khodabakhshi, Z., Hosseinkhah, N. & Ghadiri, H. Pulsating Microbubble in a Micro-vessel and mechanical effect on vessel wall: A simulation study. *J. Biomed. Phys. Eng.* <https://doi.org/10.31661/jbpe.v0i0.1131> (2020).
51. Cho, E. E., Drazic, J., Ganguly, M., Stefanovic, B. & Hynynen, K. Two-photon fluorescence microscopy study of cerebrovascular dynamics in ultrasound-induced blood–brain barrier opening. *J. Cereb. Blood Flow. Metab.* **31**, 1852–1862 (2011).
52. Sheikov, N. et al. Brain arterioles show more active vesicular transport of blood-borne tracer molecules than capillaries and venules after focused ultrasound-evoked opening of the blood-brain barrier. *Ultrasound Med. Biol.* **32**, 1399–1409 (2006).

53. Hyvelin, J.-M. et al. Characteristics and echogenicity of clinical ultrasound contrast agents: An in vitro and in vivo comparison study. *J. Ultrasound Med.* **36**, 941–953 (2017).
54. Marmottant, P. et al. A model for large amplitude oscillations of coated bubbles accounting for buckling and rupture. *J. Acoustical Soc. Am.* **118**, 3499–3505 (2005).
55. Dayton, P. A., Morgan, K. E., Klibanov, A. L., Brandenburger, G. H. & Ferrara, K. W. Optical and acoustical observations of the effects of ultrasound on contrast agents. *IEEE Trans. Ultrason. Ferroelectr. Freq. Control* **46**, 220–232 (1999).
56. Santin, M. D. et al. Encapsulated contrast microbubble radial oscillation associated with postexcitation pressure peaks. *J. Acoust. Soc. Am.* **127**, 1156–1164 (2010).
57. Tietz, S. & Engelhardt, B. Brain barriers: Crosstalk between complex tight junctions and adherens junctions. *J. Cell Biol.* **209**, 493–506 (2015).
58. Choi, J. J. et al. Microbubble-size dependence of focused ultrasound-induced blood-brain barrier opening in mice in vivo. *IEEE Trans. Biomed. Eng.* **57**, 145–154 (2010).
59. Wong, A. et al. The blood-brain barrier: an engineering perspective. *Front. Neuroeng.* **6**, 7 (2013).
60. Curley, C. T. et al. Immunomodulation of intracranial melanoma in response to blood-tumor barrier opening with focused ultrasound. *Theranostics* **10**, 8821–8833 (2020).
61. Wang, X. et al. Advances on fluid shear stress regulating blood-brain barrier. *Microvasc. Res.* **128**, 103930 (2020).
62. Cucullo, L., Hossain, M., Puvenna, V., Marchi, N. & Janigro, D. The role of shear stress in blood-brain barrier endothelial physiology. *BMC Neurosci.* **12**, 40 (2011).
63. Engelhardt, B. & Ransohoff, R. M. Capture, crawl, cross: the T cell code to breach the blood-brain barriers. *Trends Immunol.* **33**, 579–589 (2012).
64. Engelhardt, B., Vajkoczy, P. & Weller, R. O. The movers and shapers in immune privilege of the CNS. *Nat. Immunol.* **18**, 123–131 (2017).
65. Abadier, M. et al. Cell surface levels of endothelial ICAM-1 influence the transcellular or paracellular T-cell diapedesis across the blood-brain barrier. *Eur. J. Immunol.* **45**, 1043–1058 (2015).
66. Gilbert, M. R. et al. A randomized trial of bevacizumab for newly diagnosed glioblastoma. *N. Engl. J. Med.* **370**, 699–708 (2014).
67. Sonabend, A. M. et al. Repeated blood-brain barrier opening with an implantable ultrasound device for delivery of albumin-bound paclitaxel in patients with recurrent glioblastoma: a phase 1 trial. *Lancet Oncol.* **24**, 509–522 (2023).
68. Lim, M., Xia, Y., Bettgowda, C. & Weller, M. Current state of immunotherapy for glioblastoma. *Nat. Rev. Clin. Oncol.* **15**, 422–442 (2018).
69. Johnson, L. A. et al. Rational development and characterization of humanized anti-EGFR variant III chimeric antigen receptor T cells for glioblastoma. *Sci. Transl. Med.* **7**, 275ra22 (2015).
70. Genoud, V. et al. Responsiveness to anti-PD-1 and anti-CTLA-4 immune checkpoint blockade in SB28 and GL261 mouse glioma models. *Oncoimmunology* **7**, e1501137 (2018).
71. Chuntova, P. et al. Novel EGFRvIII-CAR transgenic mice for rigorous preclinical studies in syngeneic mice. *Neuro Oncol.* <https://doi.org/10.1093/neuonc/noab182> (2021).
72. Kerfoot, S. M. et al. Reevaluation of P-selectin and $\alpha 4$ integrin as targets for the treatment of experimental autoimmune encephalomyelitis. *J. Immunol.* **176**, 6225–6234 (2006).
73. Battistini, L. et al. CD8+ T cells from patients with acute multiple sclerosis display selective increase of adhesiveness in brain venules: a critical role for P-selectin glycoprotein ligand-1. *Blood* **101**, 4775–4782 (2003).
74. Steiner, O. et al. Differential roles for endothelial ICAM-1, ICAM-2, and VCAM-1 in shear-resistant T cell arrest, polarization, and directed crawling on blood-brain barrier endothelium. *J. Immunol.* **185**, 4846–4855 (2010).
75. Arvanitis, C. D., Ferraro, G. B. & Jain, R. K. The blood-brain barrier and blood-tumour barrier in brain tumours and metastases. *Nat. Rev. Cancer* **20**, 26–41 (2020).
76. McMahon, D., Lassus, A., Gaud, E., Jeannot, V. & Hynynen, K. Microbubble formulation influences inflammatory response to focused ultrasound exposure in the brain. *Sci. Rep.* **10**, 21534 (2020).
77. Meng, Y. et al. MR-guided focused ultrasound liquid biopsy enriches circulating biomarkers in patients with brain tumors. *Neuro Oncol.* <https://doi.org/10.1093/neuonc/noab057> (2021).
78. Pacia, C. P. et al. Focused ultrasound-mediated liquid biopsy in a tauopathy mouse model. *Radiology* **307**, e220869 (2023).
79. Zhao, S. et al. Radiation-force assisted targeting facilitates ultrasonic molecular imaging. *Mol. Imaging* **3**, 135–148 (2004).
80. Miller, M. W., Miller, D. L. & Brayman, A. A. A review of in vitro bioeffects of inertial ultrasonic cavitation from a mechanistic perspective. *Ultrasound Med. Biol.* **22**, 1131–1154 (1996).
81. Kimmel, E., Krasovitski, B., Hoogi, A., Razansky, D. & Adam, D. Subharmonic response of encapsulated microbubbles: Conditions for existence and amplification. *Ultrasound Med. Biol.* **33**, 1767–1776 (2007).
82. Tu, J. et al. Microbubble sizing and shell characterization using flow cytometry. *IEEE Trans. Ultrason. Ferroelectr. Freq. Control* **58**, 955–963 (2011).
83. Helfield, B. L. & Goertz, D. E. Nonlinear resonance behavior and linear shell estimates for Definity™ and MicroMarker™ assessed with acoustic microbubble spectroscopy. *J. Acoustical Soc. Am.* **133**, 1158–1168 (2013).
84. Chatterjee, D. & Sarkar, K. A Newtonian rheological model for the interface of microbubble contrast agents. *Ultrasound Med. Biol.* **29**, 1749–1757 (2003).
85. O'Rourke, D. M. et al. A single dose of peripherally infused EGFRvIII-directed CAR T cells mediates antigen loss and induces adaptive resistance in patients with recurrent glioblastoma. *Sci. Transl. Med.* **9**, eaaa0984 (2017).
86. Brown, C. E. et al. Regression of glioblastoma after chimeric antigen receptor T-Cell therapy. *N. Engl. J. Med.* **375**, 2561–2569 (2016).
87. Shamay, Y. et al. P-selectin is a nanotherapeutic delivery target in the tumor microenvironment. *Sci. Transl. Med.* **8**, 345ra87–345ra87 (2016).
88. Tylawsky, D. E. et al. P-selectin-targeted nanocarriers induce active crossing of the blood-brain barrier via caveolin-1-dependent transcytosis. *Nat. Mater.* **22**, 391–399 (2023).
89. van der Meer, S. et al. Microbubble spectroscopy of ultrasound contrast agents. *J. Acoustical Soc. Am.* **120**, 3327–3327 (2006).
90. Hosseinkhah, N., Chen, H., Matula, T. J., Burns, P. N. & Hynynen, K. Mechanisms of microbubble-vessel interactions and induced stresses: A numerical study. *J. Acoust. Soc. Am.* **134**, 1875–1885 (2013).
91. Guo, Y. et al. Single-cell analysis reveals effective siRNA delivery in brain tumors with microbubble-enhanced ultrasound and cationic nanoparticles. *Sci. Adv.* **7**, eabf7390 (2021).
92. Bader, K. B. & Holland, C. K. Gauging the likelihood of stable cavitation from ultrasound contrast agents. *Phys. Med. Biol.* **58**, 127–144 (2013).
93. Pulkkinen, A., Huang, Y., Song, J. & Hynynen, K. Simulations and measurements of transcranial low-frequency ultrasound therapy: skull-base heating and effective area of treatment. *Phys. Med. Biol.* **56**, 4661 (2011).
94. Choi, J. J., Pernot, M., Brown, T. R., Small, S. A. & Konofagou, E. E. Spatio-temporal analysis of molecular delivery through the blood-brain barrier using focused ultrasound. *Phys. Med. Biol.* **52**, 5509 (2007).

95. Seo, H., Huh, H., Lee, E.-H. & Park, J. Numerical evaluation of the effects of transducer displacement on transcranial focused ultrasound in the rat brain. *Brain Sci.* **12**, 216 (2022).
96. Fritz-Hansen, T. et al. Measurement of the arterial concentration of Gd-DTPA using MRI: A step toward quantitative perfusion imaging. *Magn. Reson. Med.* **36**, 225–231 (1996).
97. The Gene Ontology Consortium, Aleksander, S. A. et al. The Gene Ontology knowledgebase in 2023. *Genetics* **224**, iyad031 (2023).
98. Ashburner, M. et al. Gene Ontology: tool for the unification of biology. *Nat. Genet* **25**, 25–29 (2000).

Acknowledgements

We thank Dr. Johannes Leisen at Georgia Tech's Magnetic Resonance Imaging Core (MRI) facility for providing outstanding technical support during MRI studies. We also thank Dr. Anton Bryksin, Shweta Biliya, and Naima Djeddar at Georgia Tech's Molecular Evolution Core for their valuable support in RNA sequencing. This study was supported by NIH grants R37 CA239039 (C.A.) R01CA273878 (C.A.). This study was also supported by the Parker Institute for Cancer Immunotherapy (H.O.) and Ians Friends Foundation (C.A. and H.O.). H.O. was supported by NIH/NINDS grant R35NS105068. M.O.B was supported by Leducq Foundation grant 17 CVD 03, and the Engineering and Physical Sciences Research Council grant EP/X025705/1. H.J. was supported by the NIH grants HL119798, HL139757, and HL151358. H.J. was also supported by Wallace H. Colter Distinguished Faculty Chairship. Y.G. was partially supported by the Focused Ultrasound Foundation Lockhart Postdoctoral Fellowship. C.P. was supported by NIH grant T32HL166146. M.G. was supported by the German Research Foundation (GA 3535/1-1).

Author contributions

Y.G., H.L., and C.A. conceived and designed the experiments; Y.G., H.L., C.K., and C.A. performed the experiments; Y.G., H.L., C.K., M.G., and C.P. analyzed the data; A.Y., P.C., H.J., H.O., contributed materials/analysis tools; Y.G., H.L., C.K., C.P., M.G., H.O., H.J., M.O.B and C.A. wrote the paper. All authors reviewed the manuscript and approved the final version.

Competing interests

The authors declare no competing interests.

Additional information

Supplementary information The online version contains supplementary material available at <https://doi.org/10.1038/s41467-024-52329-y>.

Correspondence and requests for materials should be addressed to Costas Arvanitis.

Peer review information *Nature Communications* thanks Anuska Andjelicovic, Anthony Novell, and Man Lu for their contribution to the peer review of this work. A peer review file is available.

Reprints and permissions information is available at <http://www.nature.com/reprints>

Publisher's note Springer Nature remains neutral with regard to jurisdictional claims in published maps and institutional affiliations.

Open Access This article is licensed under a Creative Commons Attribution-NonCommercial-NoDerivatives 4.0 International License, which permits any non-commercial use, sharing, distribution and reproduction in any medium or format, as long as you give appropriate credit to the original author(s) and the source, provide a link to the Creative Commons licence, and indicate if you modified the licensed material. You do not have permission under this licence to share adapted material derived from this article or parts of it. The images or other third party material in this article are included in the article's Creative Commons licence, unless indicated otherwise in a credit line to the material. If material is not included in the article's Creative Commons licence and your intended use is not permitted by statutory regulation or exceeds the permitted use, you will need to obtain permission directly from the copyright holder. To view a copy of this licence, visit <http://creativecommons.org/licenses/by-nc-nd/4.0/>.

© The Author(s) 2024